An atmospheric source of S in Mesoarchaean structurally-controlled gold mineralisation of the Barberton Greenstone Belt

Authors**:** Andrea Agangi[1]*, Axel Hofmann[2], Benjamin Eickmann[2], Johanna Marin-Carbonne[3], Steven M. Reddy[1]

[1] Department of Applied Geology, Curtin University, Bentley, WA, Australia.

[2] Department of Geology University of Johannesburg, Johannesburg, South Africa

[3] Université Lyon – UJM –Saint Etienne- Laboratoire Magma et Volcans CNRS UMR 6524-,UBP, IRD – 23 rue Paul Michelon 42100 St Etienne

Keywords: Archaean; gold; Barberton Greenstone Belt; multiple S isotopes

*andrea.agangi@curtin.edu.au

An atmospheric source of S in Mesoarchaean structurally-controlled gold mineralisation of the Barberton Greenstone Belt

Keywords: Archaean, gold, Barberton Greenstone Belt, multiple S isotopes

Abstract

The Barberton Greenstone Belt of southern Africa hosts several Mesoarchaean gold deposits. The ores were mostly formed in greenschist facies conditions, and occur as hydrothermal alteration zones around extensional faults that truncate and post-date the main compressional structures of the greenstone belt. Ore deposition was accompanied by the intrusion of porphyries, which has led to the hypothesis that gold may have been sourced from magmas. Because the transport of Au in the hydrothermal fluids is widely believed to have involved S complexes, tracing the origin of S may place strong constraints on the origin of Au. We measured multiple S isotopes in sulfide ore from Sheba and Fairview mines of the Barberton Greenstone Belt to distinguish "deep" S sources (e.g. magmas) from "surface" S sources (i.e. rocks of the volcano-sedimentary succession that contain S processed in the atmosphere preserved as sulfide and sulfate minerals). Ion probe (SIMS) analyses of pyrite from ore zones indicate mass-independent fractionation of S isotopes ($\Delta^{33}S$ = -0.6 – +1.0 ‰) and the distribution of the analyses in the $\Delta^{33}S - \delta^{34}S$ space matches the distribution peak of previously published analyses of pyrite from the entire volcano-sedimentary succession. Notwithstanding that the H_2O-CO_2 components of the fluids may have been introduced from a deep source external to the greenstone belt rocks, the fact that S bears an atmospheric signature suggests the hypothesis that the source of Au should also be identified in the supracrustal succession of the greenstone belt. Our findings differ from conclusions of previous studies of other Archaean shear-hosted Au deposits based on mineralogical and isotopic evidence, which suggested a magmatic or mantle source for Au, and imply that there is no single model that can be applied to this type of mineralisation in the Archaean.

1. Introduction

The Palaeoarchaean Barberton Greenstone Belt of southern Africa hosts some of the oldest gold mineralisation known (Anhaeusser, 1976; de Ronde et al., 1991; Dirks et al., 2013; Dziggel et al., 2010) (Fig 1). These deposits have proved to be an important source of Au since their discovery in the 1880s, and have produced more than 345 tons of Au (Anhaeusser, 1976; Dirks et al., 2009) (Fig 1). Most deposits are hosted in greenschist facies rocks, where gold mineralisation is structurally controlled and occurs along extensional faults cross-cutting the main compressional structures of the greenstone belt, which extend for several tens of km along strike (Dirks et al., 2013). The ore is

dominated by pyrite and arsenopyrite, and gold is mostly finely dispersed in sulfides, either present in the mineral structure or as sub-microscopic inclusions ("invisible gold") (Craig et al., 1998). In this kind of structurally-controlled gold deposits, the mineralising fluids are typically aqueo-carbonic and have low to moderate salinity (Goldfarb et al., 2001; Mikucki and Ridley, 1993), and are interpreted to originate from a deep source (Salier et al., 2005). The origin of mineralising fluids is controversial, especially in Archaean deposits, and mineralogical, elemental and isotopic evidence seems to point towards either metamorphic or igneous sources, or a combination of these (Hutti mine, India; Rogers et al., 2013; Western Australia, Doublier et al., 2014; Wang et al., 1993). Propagation of these fluids along crust-scale structures is believed to be responsible for the formation of deposits in a single region over a range of depths and temperatures (from <200 to >500, and possibly ≤700°C) ("crustal continuum model"; Barnicoat et al., 1991; Groves, 1993; Phillips and Powell, 2009; Kolb et al., 2015). Deposition of Au would have occurred by reaction of the mineralising fluid with the host rocks or by fluid mixing (Bateman and Hagemann, 2004; Evans et al., 2006), or vapour separation (de Ronde et al., 1992; Mikucki and Ridley, 1993). The origin of S is an important aspect in the study of deposits hosted in Archaean greenstone belts and other structurally controlled Au deposits, since hydrosulfide complexes [$Au(HS)_2^-$ and AuHS] are believed to be the main Au transporting agents (Benning and Seward, 1996; Pokrovski et al., 2014; Seward, 1973; Simon et al., 1999). Therefore, identifying the source of S can help constrain the origin of Au in these deposits, which has so far remained elusive (Tomkins, 2013; Gaboury, 2013; Kendrick et al., 2011; Pitcairn 2006).

In order to distinguish deep (magmatic- or mantle-related) from sedimentary sources of sulfur, multiple S isotope analyses can be used. Mass-independent fractionation of S isotopes (MIF-S) is a common feature of Archaean and early Palaeoproterozoic (>2.4 Ga) sedimentary and diagenetic sulfur minerals (sulfides and sulfates; Ono et al., 2003). This S isotope signature is believed to originate from ultraviolet radiation-induced reactions of S gas species (e.g. SO_2, SO_3) in anoxic atmosphere, and thus to be a distinctively atmospheric signature (e.g. Farquhar et al., 2000). MIF-S can be expressed as $\Delta^{33}S = \delta^{33}S - 1000 \cdot [(1 - \delta^{34}S/1000)^{0.515} - 1]$, as ‰ variation. Among the products of this reaction, water-soluble sulfate with $\Delta^{33}S < 0$ and relatively insoluble elemental S with $\Delta^{33}S > 0$ can then be separated by bodies of water upon deposition on the Earth's surface, incorporated into the sediments, and preserved in the rock record in the form of sulfide and sulfate minerals. In the Barberton Greenstone Belt MIF-S has been described in pyrite and barite from several stratigraphic units (Grosch and McLoughlin, 2013; Montinaro et al., 2015; Philippot et al., 2012; Roerdink et al., 2012; 2013).

Following the discovery of MIF-S in sedimentary environments, MIF-S signal has also been found in Neoarchaean VMS deposits (Jamieson et al., 2013), in diamond-hosted sulfide inclusions (Farquhar et al., 2002; Thomassot et al., 2009), in the Palaeoproterozoic Rustenburg Layered Suite of the Bushveld complex (Penniston-Dorland et al., 2012) and in olivine-hosted sulfide inclusions in Cainozoic plume-related ocean island basalt magmas (Cabral et al., 2013). These findings have revealed a feedback between surface and deep S cycle, indicating that S processed in the atmosphere during the Archaean can be stored in the crust or the mantle, and be recycled back to the surface through different processes, even after a long time. Thus, using MIF-S signal as a marker of Archaean atmospheric processes has opened up new ways of testing the hypothesis that ore deposits, even if non-sediment-hosted, can have sourced at least part of their S from sediments or other deposits that carry MIF-S (Bekker et al., 2009; Fiorentini et al., 2010; 2012; Hofmann et al., 2014).

In this study, analyses of multiple S isotopes (^{32}S, ^{33}S, ^{34}S) have been used to trace the origin of S in structurally controlled hydrothermal Au deposits of the Barberton Greenstone Belt by comparing the S isotope compositions of the ore and sulfide and sulfate minerals hosted throughout the volcano-sedimentary succession. The analysis of multiple S isotopes offers advantages, as different processes affecting hydrothermal fluids, such as redox reactions and fluid-phase separation can impart significant mass-dependent fractionation of S isotopes, and modify the original $\delta^{34}S$ composition. Also, because of the limited variation of $\delta^{34}S$ during the Archaean, and because post-depositional processes, e.g. metamorphism, can mask original isotopic variations, in many cases $\delta^{34}S$ alone cannot unambiguously identify the origin of S. In contrast, metamorphic reactions and hydrothermal remobilisation would have limited impact on $\Delta^{33}S$ values except in the case where mineralisation involves mixing of S pools with different $\Delta^{33}S$.

2. Geological setting

The Palaeoarchaean Barberton Greenstone Belt is situated in the east of the Kaapvaal Craton, southern Africa (Fig 1). Its volcano-sedimentary succession, the ca. 3.55 – 3.22 Ga old Barberton (or Swaziland) Supergroup (Anhaeusser, 1976) is preserved in a southwest-northeast-trending belt surrounded by granitoid rocks, and has been divided into three main lithostratigraphic units: the Onverwacht Group, the Fig Tree Group, and the Moodies Group, in ascending order (Lowe and Byerly, 2007; Viljoen and Viljoen, 1969). The Onverwacht Group is mostly composed of komatiite, komatiitic basalt and basalt, with minor felsic volcanic rocks, and has been dated at ca. 3550 – 3300 Ma (Kröner et al., 1996). The Fig Tree and Moodies groups consist of sandstone, shale, chert, banded iron formation and felsic volcanic rocks, and have been dated at ca. 3260 – 3216 Ma (Byerly et al.,

1996; de Ronde and de Wit, 1994; Hofmann, 2005; Kamo and Davis, 1994; Kröner et al., 1991). The southwest to northeast-trending Inyoka-Saddleback Fault System, separates a northern and a southern terrane of different age and geochemical characteristics (Kamo and Davis, 1994; Kisters et al., 2003). Economic gold mineralisation is mainly present in the northern terrane (Fig 1).

The Barberton Supergroup has been metamorphosed under conditions of greenschist to amphibolite facies, and shows a temperature gradient, with temperatures increasing towards the margins of the belt (Dziggel et al., 2005). Three major tectono-magmatic events have affected the northern terrane. The first event is connected with accretion and collision of the southern and northern terranes at 3229 – 3227 Ma (de Ronde and Kamo, 2000; Schoene et al., 2008), and coincided with emplacement of tonalite-trondhjemite-granodiorite (TTG) intrusions, such as the Kaap Valley Tonalite (Kamo and Davis, 1994; Kisters et al., 2010). This is the main compressional event (D2 at the greenstone belt scale). The second event (event D3 at the regional scale) extending between 3.26 and 3.1 Ga, marked the passage from a compressive regime to a transtensional regime. The last event (D4, at ~3.1Ga) involved strike-slip and normal faulting, and was accompanied by emplacement of potassic granite, such as the 3106 ±3 Ma Nelspruit Batholith (de Ronde and de Wit, 1994; Kamo and Davis, 1994).

All major greenschist-facies gold deposits in the Barberton Greenstone Belt have common distinctive alteration characteristics and structural style, and occur as auriferous quartz-carbonate veins and sulfide bodies (Agangi et al., 2014; Anhaeusser, 1986; Schouwstra, 1995). Ore assemblages include predominant pyrite and arsenopyrite, with minor chalcopyrite, Ni-As sulfide and sphalerite. Most gold is hosted by sulfides as “invisible” (or refractory) gold and micro-inclusions, but free gold associated with quartz veins is also present (Cabri et al., 1989; de Ronde et al., 1992; Barberton Gold Mines, 2014). Gold mineralisation is hosted by different lithologies, ranging from meta-mafic-ultramafic rocks of the uppermost Onverwacht Group, to meta-sediments (greywacke, shale, sandstone) of the Fig Tree and Moodies groups. Alteration zones associated with greenschist-facies mineralisation in mafic-ultramafic host include, from distal to proximal to the ore, talc-carbonate, quartz-carbonate, fuchsite-quartz-carbonate ±sulfides, and sericite-quartz-sulfides ±carbonate ±fuchsite (Schouwstra, 1995). In contrast, mineralisation at New Consort mine is hosted in medium metamorphic grade rocks, and has distinct ore assemblages, which resulted from a two-stage metamorphism and mineralisation history (Otto et al., 2007).

Fluid inclusion studies from the major deposits indicate predominant low-salinity (NaCl eq = 5 – 6 wt.%), H_2O-CO_2-rich fluids, and homogenisation temperatures in the T = 290 – 310˚C range (de Ronde et al., 1992; also see Marin-Carbonne et al., 2011). Based on O, H and C isotope analyses of

mineralisation-related quartz and carbonate, the ore fluid would have had narrow ranges of $\delta^{18}O_{H2O}$ (+4.7 to 5.8 ‰), $\delta^{13}C$ (-4.5 to -2 ‰) and δD (-35 to -41 ‰), recalculated at 300°C (de Ronde et al., 1992). Hydrothermal sulfides have slightly positive $\delta^{34}S$ (+1.2 – +3.9‰ for pyrite and arsenopyrite; de Ronde et al., 1992; Kakegawa and Ohmoto, 1999). Gold is spatially associated with thrust faults associated with the main compression event at the greenstone belt scale and has been, therefore, classified as "orogenic gold" (Otto et al., 2007).On the basis of detailed structural work at Sheba and Fairview mines, Dirks et al. (2009) pointed out that gold mineralisation occurs in extensional structures cross-cutting the thrust faults. This may not apply to New Consort mine, where mineralisation is hosted in medium metamorphic grade rocks (Otto et al., 2007). At Fairview mine a 3126 ±21 Ma (U-Pb zircon dating) granitic dyke predating the shearing and mineralisation gives a maximum age for mineralisation, and 3084 ±18 Ma hydrothermal rutile may be coeval with gold mineralisation (de Ronde et al., 1991). Dating of syn-mineralisation dykes at New Consort mine (3030 – 3040 Ma, U – Pb zircon) and Golden Quarry near Sheba mine (3015 – 3100 Ma, Pb – Pb zircon; Dirks et al., 2013), and dating of titanite associated with sulfides at 3027 Ma at New Consort mine (Dziggel et al., 2010) suggests that Au deposition may have lasted for several tens of million years. This seems to imply a protracted, multi-stage mineralisation process (Dziggel et al., 2010).

3. Sample preparation and analytical methods

Samples collected from Fairview and Sheba mines were prepared as polished rock chip mounts and thin sections and observed by conventional optical microscopy and scanning electron microscopy (SEM). SEM observations were made using a Tescan Vega 3 SEM equipped with energy-dispersion spectroscopy (EDS) detector at the Spectrum Centre of the University of Johannesburg. Additional EDS and electron backscatter diffraction (EBSD) data were collected at Curtin University on a Mira Tescan FE-SEM. X-ray element distribution maps were obtained using a four spectrometer-equipped Cameca SX-100 electron microprobe. Arsenic (Lα line), Co (Kα), Ni (Kα), and Pb (Mα) for pyrite, and Co (Kα), Ni (Kα), Se (Lα), and Sb (Lα) for arsenopyrite, were measured at 20 kV acceleration, 80 nA beam current. See Agangi et al. (2015) for full analytical details.

In situ S isotope analyses (SIMS)

Sulfur isotope compositions ($\delta^{34}S$ and $\delta^{33}S$) were measured by secondary ion mass spectrometry (SIMS) using a Cameca ims 1280 HR2 at CRPG-CNRS (Nancy, France). The analytical method is described in detail in Thomassot et al. (2009) and only summarized here. Briefly, a Cs^+ primary beam of 5 nA intensity was focused to a spot of about 15-20 µm. ^{32}S, ^{33}S and ^{34}S were simultaneously measured in three off-axis Faraday cups (L'2, C and H1). The relative gains of the

Faraday cups were intercalibrated at the beginning of the analytical session. Typical ^{32}S intensity was between 1 and $7 \cdot 10^8$ counts per second (cps). Several sulfide in-house reference minerals (Maine, Spain and Balmat; Marin-Carbonne et al., 2014) were used to determine the instrumental mass fractionation and the reference mass discrimination line, from which $\Delta^{33}S$ was calculated. A typical analysis consisted of 2 minutes of pre-sputtering followed by 30 cycles of 3 s each. The background of each detector was measured during the pre-sputtering and was then corrected for each analysis. The internal precision achieved in these conditions was better than 0.06 ‰ for $\delta^{34}S$ and better than 0.10 ‰ for $\delta^{33}S$ (2σ). The reproducibility, based on multiple measurements of the reference materials, for $\delta^{34}S$ was ± 0.40 ‰ (2σ), and the reproducibility for $\Delta^{33}S$ was ±0.06 (2σ). Sulfur isotopes are expressed as per mil (‰) variation relative to the Vienna Canyon Diablo Troilite (VCDT) international reference, as $\delta^{3x}S = 1000 \cdot [(^{3x}S/^{32}S)_{sample} - (^{3x}S/^{32}S)_{VDVT}/(^{3x}S/^{32}S)_{VCDT}]$. Deviations from linear relations between $\delta^{33}S$ and $\delta^{34}S$ reflect mass-independent fractionation (MIF), and can be expressed as $\Delta^{33}S = \delta^{33}S - 1000 \cdot [(1 - \delta^{34}S/1000)^{0.515} - 1]$, as per mil variation. The results are reported in Additional Tables 1 and 2.

4. Sample description and sulfide chemical zoning

Samples 46CMR and 62-11 were collected at Fairview mine (Fig 1B). Sample 46CMR was collected from the Commitment Reef, in rocks belonging to the Fig Tree Group, between the Eureka syncline and Ulundi syncline, east of the Sheba fault (Fig 1B). Sample 46CMR is a fine-grained foliated rock (metagreywacke), mostly composed of oriented colourless phyllosilicate (muscovite), quartz, Fe-Mg carbonate, and µm-scale anhedral grains of monazite. The sample is cross-cut by quartz-carbonate veins up to ~1 cm wide. Sample 62-11 is representative of sulfide mineralisation at the contact between chert and greywacke at Fairview mine, and part of a 6 m-wide zone of high grade Au mineralisation (30-40 g/ton Au). Stockwork quartz and Fe-Ca-Mg carbonate veins cross-cut the chert host rock. In both sample 46CMR and 62-11, mineralisation is composed of euhedral to anhedral pyrite, arsenopyrite and minor chalcopyrite, gersdorffite, sphalerite and native gold, which occur associated with quartz-carbonate veins (Fig 2A). Arsenopyrite forms randomly-oriented, elongate euhedral grains overgrowing pyrite (Fig 2B). Pyrite contains inclusion-rich (mostly silicate inclusions) and massive-textured domains, which are either concentrically or irregularly distributed within single pyrite grains. In addition, some anhedral and inclusion-rich pyrite grains have textures reminiscent of pyrite of diagenetic origin (Fig 2C).

Samples 33ZK-A and 33ZK-B, collected at Sheba mine, are representative of mineralisation in the Zwartkoppie reef, which is located at the top of the Onverwacht Group (Dirks et al., 2009; Wagener and Wiegand, 1986). The samples include quartz-carbonate-sulfide veins in strongly

deformed and silicified (ultra)mafic volcanic rocks and chert. The rock is foliated at the mm-scale, and mostly composed of alternating dark grey fine-grained microcrystalline quartz-rich layers (chert) and green, foliated quartz-fuchsite (Cr-bearing muscovite)-carbonate-rich schist. Ore minerals include pyrite, chalcopyrite, ullmannite [Ni(Sb,As)S], gersdorffite, and sphalerite. Pyrite occurs as 1) euhedral to subhedral crystals, up to 100-200 µm in size (Fig 2D), which occur in, or at the contact with, quartz-carbonate veins; and 2) anhedral crystals, up to 500 µm, occurring in aggregates with chalcopyrite, ullmannite, and gersdorffite.

Chemical zoning of pyrite and arsenopyrite

High-contrast BSE images and X-ray compositional maps of pyrite from Fairview mine reveal complex growth patterns, which indicate different events of crystal growth, veining, resorption and crystallisation (Fig 3). Recrystallised domains of pyrite are typically associated with deposition of gold and other sulfides, including arsenopyrite, gersdorffite, sphalerite, chalcopyrite and galena (Fig 3, Additional Fig 1). This is also visible in inclusion-rich pyrite crystals, which have massive overgrowths and intragranular textures associated with sulfide inclusions that suggest recrystallisation and element remobilisation as shown by trace element X-ray maps (Fig 4). In contrast, arsenopyrite has simpler intragranular textures, with concentric element zoning (Se, Sb) and in some cases cross-cutting Ni-rich veinlets (Additional Fig 2). Elemental maps of pyrite from Sheba mine indicate complex textures indicative of a multi-stage depositional mechanism, similar to what was found in samples from Fairview mine (Additional Fig 3).

5. Multiple S isotope analyses

Pyrite analyses revealed mostly positive $\delta^{34}S$ values (-0.87 to +9.64 ‰), and $\Delta^{33}S$ values varying from -0.6 to +1.0 ‰ (with the exception of one outlying analysis at -1.97 ‰) (Fig 5, Additional Table 1). The histogram of $\Delta^{33}S$ has a near-symmetric distribution and a peak around 0 (Fig 5B). The histogram of $\delta^{34}S$ has a peak between +4 and +5 ‰ for pyrite. A comparison with published multiple S isotopes from the Barberton Greenstone Belt indicates that these values largely overlap with the S isotope values of sediment-hosted and volcanic-hosted sulfides. No clear correlation was found between texture of pyrite (inclusion-rich vs. massive) and S isotope compositions. Some of the highest $\Delta^{33}S$ values were found in euhedral hydrothermal pyrite grains from Sheba mine that show euhedral zoning in BSE images (Fig 6). Significant variations in $\delta^{34}S$ and $\Delta^{33}S$ can be observed, even in adjacent spots on single grains (e.g. $\Delta^{33}S$ varying from 1.0 to 0.2 ‰ within 50 µm distance, Fig 6A).

6. Discussion

6.1. Structurally-controlled Au deposits, genetic models and possible sources of S-bearing auriferous fluids

Structurally-controlled Au deposits, also referred to as orogenic or shear-hosted Au deposits, include a variety of Au deposits that formed in accreted and metamorphosed terranes and may have been formed by fluids derived from crustal sources (e.g. devolatilisation of a volcano-sedimentary succession during metamorphism) or from subcrustal sources (e.g. mantle-derived magmas and fluids; Goldfarb and Groves, 2015; Pitcairn et al., 2006; Yardley and Cleverley, 2013). The problem of fluid source is a complex one, especially in old terranes that have undergone multiple tectono-thermal and magmatic events during their history, and much effort has been placed in addressing this issue (Lüders et al., 2015; Mikucki and Ridley, 1993). Various hypotheses have been proposed to explain the origin of fluids (and, by inference, S and Au) in Archaean and Proterozoic gold deposits, including, 1) metamorphic dehydration of the crust (Groves and Phillips, 1987), 2) derivation from felsic magmas (Cameron and Hattori, 1987; Salier et al., 2005 and refs therein), or a combination of these (; Wulff et al., 2010), and 3) mantle derivation associated with alkaline magmatism (Phillips and Powell, 2009) or mantle degassing and granulitisation (Cameron, 1988; Fu and Touret, 2014). In the following discussion, we evaluate the significance of our results in the light of the existing genetic models.

6.2 Crustal origin for the mineralising fluids

The rocks of the Barberton Supergroup represent the most immediate source of MIF-S. These rocks are known to contain S phases recording wide variations of $\Delta^{33}S$ and $\delta^{34}S$ ($\Delta^{33}S$ of pyrite ranges mostly from -1.3 to +4.2 ‰, occasionally up to +14 ‰, and $\delta^{34}S$ ranges from -55 to +29 ‰). Figure 5 represents the $\Delta^{33}S$ versus $\delta^{34}S$ plot of a dataset of approximately 1700 published analyses of pyrite, barite and bulk-rock samples from across the Barberton Supergroup, ranging in age from 3.5 to 3.2 Ga. The distribution density of these analyses, which can be obtained by counting the number of analyses per unit cell in the $\delta^{34}S$ vs $\Delta^{33}S$ space, allows to identify the most commonly represented compositions. A very distinct density peak can be seen centred at around $\Delta^{33}S$ ~0‰ and $\delta^{34}S$ ~1.5‰. Assuming that the dataset is representative of the S composition of the Barberton Greenstone Belt, high-density areas are expected to make the largest contribution of S (and other elements) to hydrothermal fluids leaching the rocks. A comparison with this dataset shows that our analyses plot remarkably close to the density peak. Thus, rocks of the volcano-sedimentary succession represent an abundant, compositionally suitable proximity source of S for the hydrothermal fluids responsible for Au mineralisation at Sheba and Fairview.

When considering in further detail the possible sources of S to the mineralising fluids, it becomes apparent that the distribution of our analyses in the $\delta^{34}S - \Delta^{33}S$ space is mostly comparable to a distinctive steep negative trend observed in different studies of pyrite from barite-free samples of the Barberton Greenstone Belt (Philippot et al., 2012; Roerdink et al., 2013), and replicated in bulk-rock analyses of shales containing finely-disseminated pyrite in both the Fig Tree and Moodies groups, which host the mineralisation (Montinaro et al., 2015) (Fig 5). Roerdink et al. (2013) reported this negative trend in different sedimentary rocks, including conglomerate, chert, breccia and dolomite. A similar trend was reported in pyrite from the 3.5 Ga old Dresser Formation of the Pilbara craton (Philippot et al., 2007) and in pyrite nodules from ca. 2.7 Ga old shales of the Eastern Goldfields of the Yilgarn craton (Steadman et al., 2015). This trend may be either due to redox reactions and local mixing of S pools with different $\Delta^{33}S$ compositions (Roerdink et al., 2013) or represent an atmospheric fractionation array (Philippot et al., 2012). Values of $\Delta^{33}S$ in these analyses are mostly positive, but also extend to negative values (as low as -0.7 ‰), encompassing the entire range of our analyses. Shales are considered a good source of S and Au in Phanerozoic orogenic Au deposits (e.g. Pitcairns, 2006). In these rocks, Au is typically trapped by sedimentary to diagenetic pyrite and is remobilised upon destabilisation of pyrite during metamorphism (Hu et al., 2016; Thomas et al., 2011; Tomkins et al., 2010). Evidence of high Au concentrations in diagenetic pyrite in the Neoarchaean (up to 3 – 4 ppm; Steadman et al., 2015) opens up the possibility that this may also apply to Archaean successions.

Negative $\Delta^{33}S$ are known from rocks and mineral deposits interpreted to have interacted with sea water sulfate, such as volcanic-hosted massive sulfide (VMS) deposits and sea floor-altered volcanic rocks (Bekker et al., 2009; Jamieson et al., 2013; Fiorentini et al., 1012). Mafic and ultramafic magmas are known to be relatively Au-rich, and are considered as the main source of Au in some Neoarchean orogenic Au deposits, such as the ones in the Yilgarn craton of Western Australia (Groves and Phillips, 1987; Bierlein and Pisarevsky, 2008). In the Barberton Greenstone Belt, mafic-ultramafic volcanic rocks from the Onverwacht Group have been reported to have $\Delta^{33}S$ = -0.2 – -0.4‰, and VMS mineralisation with $\Delta^{33}S$ = -0.1 – -0.2‰ is known at Bien Venue, northeast of Sheba and Fairview mines (Montinaro et al., 2015; Fig 5). Mafic-ultramafic rocks are a largely-available source of S with negative $\Delta^{33}S$ in the Barberton Greenstone Belt, where they form the bulk of the Onverwacht Group (Fig 5). VMS ore may also have contributed S with negative $\Delta^{33}S$ signal, although the small volume of known VMS in the Barberton Greenstone Belt suggests that its contribution would have been limited.

6.3 Derivation of Au mineralising fluids from felsic magmatism

The hypothesis of a magmatic origin for mineralising fluids has been proposed in several cases of Archaean Au deposits. For example, in structurally-controlled Neoarchaean Au deposits of Western Australia, the case for magmatic derivation of ore fluids is based on several lines of evidence, such as the presence of coeval magmatism (Doublier et al., 2014; Wang et al., 1993), trace element signature of accessory minerals (Bath et al., 2013), and Pb and noble gas isotope studies (Qiu and McNaughton, 1999; Kendrick et al., 2011). Although a magmatic derivation of Au mineralising fluids is not universally accepted (Goldfarb and Groves, 2015), this hypothesis has been particularly applied to Archaean deposits (Tomkins, 2013). Xue et al. (2013) have analysed multiple S isotopes of sulfide from the Eastern Goldfields of Western Australia and the Abitibi greenstone belt of Canada and, in contrast with our results, found little evidence for MIF-S from ore sulfides, thus proposing a felsic igneous or mantle source for S and, by inference, the fluids. However, although this is the simplest hypothesis, it should be noted that mixing of S pools with positive and negative $\Delta^{33}S$ will result in partial or total dilution (or "cancelling") of the MIF-S signal, so the absence of MIF-S does not conclusively rule out the possibility of sourcing of S from an "atmospheric" reservoir.

In the Barberton Greenstone Belt, involvement of magmatism has long been proposed, based on spatial and temporal associations (Anhaeusser, 1976, 1986). Widespread K-rich felsic magmatism occurred between ca. 3.11 and 3.07 Ga (such as the 3106 Ma Nelspruit Batholith to the north of the greenstone belt, or the 3105 – 3092 Ma Mpuluzi and 3107 Ma Piggs Peak Batholiths to the southwest and southeast, and the 3180 – 3067 Ma Stentor pluton; Kamo and Davis, 1994), a time span that partially overlaps with the expected age of mineralisation. . In addition, at most mines, mineralisation is spatially associated with small-volume granitic dykes (porphyries), some of which pre-date and others post-date the mineralisation (Dirks et al., 2013; Dziggel et al., 2010; Harris et al., 1995). Thus, based on intersection relationships and available radiometric ages, the mineralisation seems to have mostly postdated the main magmatic event at around 3.1 Ga, but was accompanied by emplacement of small granitic dykes. However, the role of these dykes in the mineralising process is not clear. Furthermore, the expected S isotopic composition of magmatic fluids, having near-zero $\Delta^{33}S$ and $\delta^{34}S$, makes these intrusions unlikely sources of S and mineralising fluids.

6.4 Subcrustal sources of S-bearing auriferous fluids

The idea of CO_2-rich deep fluids deriving from the mantle and flowing along crustal scale faults and tapping the lithosphere has been proposed in the past (e.g. Cameron 1988) and reproposed in recent models that aim at linking the presence of various types of Au deposits with the presence of "fertile" metasomatised lithospheric mantle (Hronsky et al., 2012; Fu and Touret, 2014). The model has been applied especially when mafic mantle magmas are coeval with mineralisation (De Boorder

2012). The pristine mantle is believed to have $\Delta^{33}S$ ~0 ‰ (Penniston-Dorland et al., 2012), although S isotope analyses of sulfides hosted in diamonds (Farquhar et al., 2002; Thomassot et al., 2009) have revealed that the sub-continental lithospheric mantle can have non-zero $\Delta^{33}S$ as a consequence of contamination from Archaean crustal material. The limited data available on these diamond-hosted sulfide samples indicate that $\Delta^{33}S$ spans from 0 to +0.6 ‰ and $\Delta^{33}S$ from ~0 to 2 ‰ (Farquhar et al., 2002), a range that is not large enough to explain our samples. More in general, in the Barberton Greenstone Belt, magmatism coeval with Au mineralisation is essentially felsic, and most likely derived from crustal melts, not from the mantle. Therefore, although involvement of sublithospheric mantle-derived fluids cannot be discounted entirely in the Barberton Greenstone Belt, it remains highly speculative at present.

As a further hypothesis, fluids deriving from a subducting slab and overlying sediments have been invoked in the Cretaceous Jiaodong Au deposits, which are hosted in high-temperature, essentially anhydrous, Precambrian rocks of the North China block (Goldfarb and Santos, 2014). In this model, fluids deriving from the devolatilisation of the subducting slab would flow up-dip along the slab-mantle boundary or percolate through the corner of the serpentinised mantle wedge eventually reaching the crust. For the Barberton Greenstone Belt, contrasting tectonic models have been presented to explain the circa 3.2 Ga compression and deformation, including modern-style subduction (Moyen et al., 2006), density-driven destabilisation of the crust and "sugduction" of the dense volcanic pile (Van Kranendonk, 2011), or modified "Archaean-type" subduction, whereby hot and weak lithosphere subducts intermittently and breaks frequently (Van Hunen and Moyen, 2012). In either case, metamorphism would result in heating and dehydration of the crust, and consequent release of MIF-S-carrying fluids. Because the source of this S would be a volcano-sedimentary succession similar to what is represented in the greenstone belt, the expected $\Delta^{33}S$ signals resulting from this type of mechanism are not different from what described previously (section 6.2).

6.5 Heterogeneous trace element and S isotope compositions as evidence for pulsating fluid

In the Barberton Greenstone Belt, Dirks et al. (2013) described mineralised brittle-ductile shear zones, which truncated compressional faults and developed in a homogeneous stress field, and concluded that mineralisation was formed during a single tectonic event. This evidence corroborates the homogeneity of fluid compositions and inferred temperatures (fluid inclusion homogenisation temperatures) and stable isotope compositions of alteration assemblages at the greenstone belt-scale, which has been interpreted as evidence for ore deposition from a single fluid of nearly constant composition (de Ronde et al., 1992). These authors suggested that the fluid responsible for the mineralisation was a H_2O-CO_2-rich fluid with salinity of 5 – 6 wt.% NaCl

equivalent that originated outside of the greenstone belt and was focussed along shear zones. However, this is seemingly in contrast with the heterogeneity of $\Delta^{33}S$ values, as well as the complex trace element zones observed in our samples. Our analyses revealed significant deviation from mass-dependent fractionation of S isotopes, with $\Delta^{33}S$ extending towards both positive and negative values ($\Delta^{33}S$ = -0.6 – +1.0 ‰). Strong microscale variations in $\Delta^{33}S$ and complex zoning textures observed in X-ray maps (overgrowth, truncation and recrystallisation, Fig 3, 4) imply that the metal content (Ni, Co, As) and S isotope composition of the mineralising fluid was heterogeneous. The different generations of pyrite generally cannot be traced across separate grains and between samples, as would be expected in large-scale, pervasive fluid flow. The values of $\delta^{34}S$ in the mineralisation can result from several reactions, such as dissolution, precipitation, fluid phase unmixing and redox reactions, all of which will impose mass-dependent fractionation on the S isotope compositions of the source. In contrast, $\Delta^{33}S$ is little affected by such processes, and variations of $\Delta^{33}S$ can only be achieved by dilution, such as leaching of sources having $\Delta^{33}S$ compositions of opposite sign. Any mixing between S pools with variable $\Delta^{33}S$ in the fluid will result in homogenisation and reduction of the overall spread of MIF-S values.

Similar overprinting textures appear to be common in structurally controlled Au deposits, and have also been described in the Neoarchaean Au deposits of Western Australia (Bateman and Hagemann, 2004). Evidence for intermittent fluid with varying temperature and composition have been presented for the Palaeoproterozoic Ashanti belt Au deposits, based on carbonate zoning and replacement textures (Mumin and Fleet, 1995). This evidence is compatible with a pulsating fluid flow (Jiang et al., 1997), and suggests that single fluid pulses had a very localised effect in terms of both S (and Au) leaching of source rocks and ore deposition. Individual fluid pulses would have transported S leached from isotopically distinct sources (i.e. different rock types as detailed above or different sulfide precursors), without large-scale mixing of S, which would have resulted in dilution of $\Delta^{33}S$ signals.

This textural and isotopic complexity is compatible with discontinuous fluid flow and sulfide cracking and replacement, as described for structurally-controlled Au deposits in the Phanerozoic, whereby shear faults are periodically reactivated when the fluid pressure overcomes the confining pressure and mineral tensile strength along the faults (fault-valve model; Sibson, 2004).

In summary, it is conceivable that “external” fluids of deep origin, magmatic or mantle-derived, fluxed through the Barberton Greenstone Belt rocks along extensional faults and remobilised S from the metamorphosed volcano-sedimentary succession, as implied by the finding of MIF-S. During discrete fluid-flow events, the fluids may have collected S from various isotopically

diverse sources, resulting in small-scale isotope heterogeneity. Modelling of ore fluid composition based on alteration assemblages in several Archaean Au deposits indicates that the fluids were S-rich, and that Au transport was primarily controlled by S complexes across the formation temperature spectrum (Phillips et al., 1996; Ridley et al., 1996). This is in agreement with the ubiquitous observation that high Au grades occur in sulfide-rich mineralisation and with the presence of finely-dispersed Au in sulfides, which implies contemporaneous deposition of S and Au. The deposition of Au is believed to occur mainly by destabilisation of S-Au complexes [$Au(HS)_2^-$ and AuHS] during wall-rock sulfidation, a mechanism compatible with the observation of invisible Au in sulfides, although H_2S extraction by fluid immiscibility (Mikucki and Ridley, 1993; Pokrovski et al., 2014), and pH and temperature variations may also have a role (Benning and Seward, 1996; Phillips et al., 1996). Therefore, the proposed distinction between the origin of S and the fluid is relevant, as a fluid originated as S-poor will not acquire its ability to carry Au until it scavenges S.

7. Conclusions

The origin of gold in structurally-controlled deposits has been a source of discussion for a long time. Part of this difficulty resides in the lithological and structural complexity of these deposits, and in the fact that the ultimate source of the fluids and Au may be far removed from the site of mineralisation. The finding of marked MIF-S in sulfide ore from the Barberton mines ($\Delta^{33}S$ varying from -0.6 to +1.0 ‰) indicates that S was previously processed through the oxygen-depleted Archaean atmosphere. In particular, a comparison between our $\delta^{34}S$ and $\Delta^{33}S$ analyses and available analyses of S isotopes from the greenstone belt suggests that S in the mineralising fluids was leached from the volcano-sedimentary succession. The $\Delta^{33}S$ <0 signal is interpreted to have derived from rocks that experienced circulation of sea water sulfate, namely sea floor-altered mafic-ultramafic volcanic rocks, and possibly VMS mineralisation. The $\Delta^{33}S$ >0 signal is interpreted to have originated from leaching of disseminated diagenetic pyrite hosted in shales, chert and conglomerate, and ultimately derived from reduction of atmospheric elemental S. These results are apparently in contrast with previous suggestions that the mineralising fluids were external to the greenstone belt and were magmatic or mantle-derived. However, as S complexes are believed to be the main complexing agent enabling the transport of Au in several cases, the problem of fluid source and the problem of S and Au source can be separated. The main components of this fluid (H_2O and CO_2; de Ronde et al., 1992) may have been introduced from an external source (e.g. felsic magmas), but would have leached S from volcanic and sedimentary rocks. Thus, this fluid would have acquired its Au-transport capability only within the greenstone belt. Therefore, S isotopes of the ore may not directly constrain the source of fluids, but have strong implications on the transport and origin of Au.

436 **Figure captions**

437 **Fig 1 A** Geological map of the Barberton Greenstone Belt and distribution of the main gold deposits
438 (modified from de Ronde et al., 1992). **B** Cross sections of Fairview and Sheba mines (modified from
439 Barberton gold mines, 2014)

440 **Fig 2** Rock textures of samples from Fairview and Sheba mines. **A** Pyrite-arsenopyrite (Asp-Py)
441 mineralisation at the contact between chert and a quartz-carbonate (Qtz, cb) vein (sample 62-11,
442 Fairview mine, transmitted plane polarised light). **B** Pyrite with euhedral arsenopyrite and Au
443 inclusions. The image was taken at high-contrast to evidence the patchy zoning of pyrite hosting
444 inclusions (sample 46CMR, BSE image). **C** Anhedral inclusion-rich pyrite aggregate with massive rim
445 (arrowed) (sample 46CMR, reflected light). **D** Euhedral pyrite with galena (Gn) secondary inclusion
446 (sample 33ZKB, Sheba mine, BSE image)

447 **Fig 3** BSE image and X-ray compositional maps of pyrite from Fairview mine. Oscillatory zones of As
448 define euhedral growth zones, truncated by irregular, As-poor and Ni-rich recrystallised pyrite.
449 Recrystallised pyrite is associated with arsenopyrite and sphalerite. Sample 46CMR-d

450 **Fig 4** Location of SIMS spot analyses overlain on BSE image of anhedral pyrite and X-ray
451 compositional maps of a portion of the pyrite showing complex intragranular textures and
452 compositional variations between inclusion-rich portion and massive rim. Pyrite contains
453 arsenopyrite, chalcopyrite and gold inclusions (BSE-brighter domains). Spots are colour-coded based
454 on $\Delta^{33}S$ values. Sample 46CMR-e, Fairview mine

455 **Fig 5** Multiple S isotope plots of pyrite from Sheba and Fairview mines. **A** and **B** Plot of $\Delta^{33}S$ vs. $\delta^{34}S$. **C**
456 Frequency histogram of $\Delta^{33}S$. The data are compared with pyrite, barite and bulk-rock analyses from
457 various units of the Barberton Greenstone Belt, some groups of literature analyses are differentiated
458 to exemplify specific data distributions. Density distribution of literature pyrite analyses was
459 calculated as number of spots per ~0.5 ‰ $\delta^{34}S$ × 0.1 ‰ $\Delta^{33}S$ cell. Literature analyses acquired with
460 different bulk and in situ methods, uncertainty up to ~0.5 ‰ $\delta^{34}S$, 0.2 ‰ $\Delta^{33}S$. References [1]
461 Philippot et al. (2012), [2] Montinaro et al. (2015), [3] Roerdink et al. (2012), [4] Bao et al. (2007), [5]
462 Roerdink et al. (2013; 2016), [6] Grosch and Mcloughlin (2013)

463 **Fig 6** BSE images and location of SIMS spot analyses of euhedral-subhedral pyrite. Spots are colour-
464 coded based on $\Delta^{33}S$ values. The two grains are located in the same thin section, around 2 mm apart.
465 Sample 33ZKA, Sheba mine

466 **Additional Fig 1** BSE image and X-ray elemental maps (sample 46CMR)

Additional Fig 2 BSE image and X-ray elemental maps of arsenopyrite. Note simple, euhedral growth textures marked by concentric zoning of elements. Sample 46CMR, Fairview mine. Sp sphalerite, Tet tetrahedrite

Additional Fig 3 BSE image, X-ray elemental maps and EBDS maps of pyrite and arsenopyrite (sample 62-11, Fairview mine)

Acknowledgement

This research was funded by SIEF (Science and Industry Endowment Fund) and the NRF (National Research Foundation of South Africa). JMC thanks the CNRS- INSU Programme National de Planétologie for their support. Johan Villeneuve is thanked for analytical assistance on the SIMS. We also acknowledge Chris Rippon (Barberton Mines (Pty) Limited) for providing the sample material used for this study.

References

Agangi, A., Hofmann, A., Przybyłowicz, W., 2014. Trace element zoning of sulfides and quartz at Sheba and Fairview gold mines: Clues to Mesoarchean mineralisation in the Barberton Greenstone Belt, South Africa. Ore Geology Reviews 56, 94-114.

Agangi, A., Przybyłowicz, W., Hofmann, A., 2015. Trace element mapping of pyrite from Archean gold deposits – A comparison between PIXE and EPMA. Nuclear Instruments and Methods in Physics Research Section B: Beam Interactions with Materials and Atoms 348, 302-306.

Anhaeusser, C.R., 1976. Archean metallogeny in southern Africa. Economic Geology 71, 16-43.

Anhaeusser, C.R., 1986. Archaean gold mineralization in the Barberton Mountain Land, in: Anhaeusser, C.R., Maske, S. (Eds.), Mineral Deposits of Southern Africa Vol.I. Geol. Soc. South Africa, pp. 113-154.

Bao, H., Rumble III, D., Lowe, D.R., 2007. The five stable isotope compositions of Fig Tree barites: Implications on sulfur cycle in ca. 3.2-Ga oceans. Geochimica et Cosmochimica Acta 71, 4868-4879.

Barnicoat, A.C., Fare, R.J., Groves, D.I., McNaughton, N.J., 1991. Synmetamorphic lode-gold deposits in high-grade Archean settings. Geology 19, 921-924.

Barberton Gold Mines, 2014. Mineral Resource & Mineral Reserve Report, 62 p. www. panafricanresources.com (consulted December 2015).

Bath, A.B., Walshe, J.L., Cloutier, J., Verrall, M., Cleverley, J.S., Pownceby, M.I., Macrae, C.M., Wilson, N.C., Tunjic, J., Nortje, G.S., Robinson, P., 2013. Biotite and apatite as tools for tracking pathways of oxidized fluids in the Archean East Repulse Gold Deposit, Australia. Economic Geology 108, 667-690.

Bateman, R., Hagemann, S., 2004. Gold mineralisation throughout about 45 Ma of Archaean orogenesis: protracted flux of gold in the Golden Mile, Yilgarn craton, Western Australia. Mineralium Deposita 39, 536-559.

Bekker, A., Barley, M.E., Fiorentini, M.L., Rouxel, O.J., Rumble, D., Beresford, S.W., 2009. Atmospheric sulfur in Archean komatiite-hosted nickel deposits. Science 326, 1086-1089.

Benning, L.G., Seward, T.M., 1996. Hydrosulphide complexing of Au (I) in hydrothermal solutions from 150–400°C and 500–1500 bar. Geochimica et Cosmochimica Acta 60, 1849-1871.

Bierlein, F.P., Pisarevsky, S., 2008. Plume-related oceanic plateaus as a potential source of gold mineralisation. Economic Geology 103, 425-430.

Byerly, G.R., Kröner, A., Lowe, D.R., Todt, W., Walsh, M.M., 1996. Prolonged magmatism and time constraints for sediment deposition in the early Archean Barberton greenstone belt: evidence from the Upper Onverwacht and Fig Tree groups. Precambrian Research 78, 125-138.

Cabral, R.A., Jackson, M.G., Rose-Koga, E.F., Koga, K.T., Whitehouse, M.J., Antonelli, M.A., Farquhar, J., Day, J.M.D., Hauri, E.H., 2013. Anomalous sulphur isotopes in plume lavas reveal deep mantle storage of Archaean crust. Nature 496, 490-493.

Cabri, L.J., Chryssoulis, S.L., de Villiers, J.P.R., Laflamme, J.H.G., Buseck, P.R., 1989. The nature of "invisible" gold in arsenopyrite. The Canadian Mineralogist 27, 353-362.

Cameron, E.M., 1988. Archean gold: Relation to granulite formation and redox zoning in the crust. Geology 16, 109-112.

Cameron, E.M., Hattori, K., 1987. Archean gold mineralization and oxidized hydrothermal fluids. Economic Geology 82, 1177-1191.

Craig, J.R., Vokes, F.M., Solberg, T.N., 1998. Pyrite: physical and chemical textures. Mineralium Deposita 34, 82-101.

de Boorder, H., 2012. Spatial and temporal distribution of the orogenic gold deposits in the Late Palaeozoic Variscides and Southern Tianshan: How orogenic are they? Ore Geology Reviews 46, 1-31.

de Ronde, C.E.J., de Wit, M.J., 1994. Tectonic history of the Barberton greenstone belt, South Africa: 490 million years of Archean crustal evolution. Tectonics 13, 983-1005.

de Ronde, C.E.J., Kamo, S., Davis, D.W., de Wit, M.J., Spooner, E.T.C., 1991. Field, geochemical and U-Pb isotopic constraints from hypabyssal felsic intrusions within the Barberton greenstone belt, South Africa: Implications for tectonics and the timing of gold mineralization. Precambrian Research 49, 261-280.

de Ronde, C.E.J., Kamo, S.L., 2000. An Archaean arc-arc collisional event: a short-lived (ca 3 Myr) episode, Weltevreden area, Barberton greenstone belt, South Africa. Journal of African Earth Sciences 30, 219-248.

de Ronde, C.E.J., Spooner, E.T.C., de Wit, M.J., Bray, C.J., 1992. Shear zone-related, Au quartz vein deposits in the Barberton greenstone belt, South Africa; field and petrographic characteristics, fluid properties, and light stable isotope geochemistry. Economic Geology 87, 366-402.

Dirks, P.H.G.M., Charlesworth, E.G., Munyai, M.R., 2009. Cratonic extension and Archaean gold mineralisation in the Sheba-Fairview mine, Barberton Greenstone Belt, South Africa. South African Journal of Geology 112, 291-316.

Dirks, P.H.G.M., Charlesworth, E.G., Munyai, M.R., Wormald, R., 2013. Stress analysis, post-orogenic extension and 3.01 Ga gold mineralisation in the Barberton Greenstone Belt, South Africa. Precambrian Research 226, 157-184.

Doublier, M.P., Thébaud, N., Wingate, M.T.D., Romano, S.S., Kirkland, C.L., Gessner, K., Mole, D.R., Evans, N., 2014. Structure and timing of Neoarchean gold mineralization in the Southern Cross district (Yilgarn Craton, Western Australia) suggest leading role of late Low-Ca I-type granite intrusions. Journal of Structural Geology 67, Part B, 205-221.

Dziggel, A., Armstrong, R.A., Stevens, G., Nasdala, L., 2005. Growth of zircon and titanite during metamorphism in the granitoid-gneiss terrane south of the Barberton greenstone belt, South Africa. Mineralogical Magazine 69, 1019-1036.

Dziggel, A., Poujol, M., Otto, A., Kisters, A.F.M., Trieloff, M., Schwarz, W.H., Meyer, F.M., 2010. New U-Pb and $^{40}Ar/^{39}Ar$ ages from the northern margin of the Barberton greenstone belt, South Africa: Implications for the formation of Mesoarchaean gold deposits. Precambrian Research 179, 206-220.

Evans, K.A., Phillips, G.N., Powell, R., 2006. Rock-buffering of auriferous fluids in altered rocks associated with the Golden Mile-style mineralization, Kalgoorlie Gold Field, Western Australia. Economic Geology 101, 805-817.

Farquhar, J., Bao, H., Thiemens, M., 2000. Atmospheric influence of Earth's earliest sulfur cycle. Science 289, 756-758.

Farquhar, J., Wing, B.A., McKeegan, K.D., Harris, J.W., Cartigny, P., Thiemens, M.H., 2002. Mass-independent sulfur of inclusions in diamond and sulfur recycling on early Earth. Science 298, 2369-2372.

Fiorentini, M.L., Barnes, S.J., Lesher, C.M., Heggie, G.J., Keays, R.R., Burnham, O.M., 2010. Platinum group element geochemistry of mineralized and nonmineralized komatiites and basalts. Economic Geology 105, 795-823.

Fiorentini, M., Beresford, S., Barley, M., Duuring, P., Bekker, A., Rosengren, N., Cas, R., Hronsky, J., 2012. District to camp controls on the genesis of komatiite-hosted nickel sulfide deposits, Agnew-Wiluna Greenstone Belt, Western Australia: Insights from the multiple sulfur isotopes. Economic Geology 107, 781-796.

Fougerouse, D., Micklethwaite, S., Tomkins, A.G., Mei, Y., Kilburn, M., Guagliardo, P., Fisher, L.A., Halfpenny, A., Gee, M., Paterson, D., Howard, D.L., 2016. Gold remobilisation and formation of high grade ore

563 shoots driven by dissolution-reprecipitation replacement and Ni substitution into auriferous arsenopyrite.
564 Geochimica et Cosmochimica Acta 178, 143-159.

565 Fu, B., Touret, J.L.R., 2014. From granulite fluids to quartz-carbonate megashear zones: The gold rush.
566 Geoscience Frontiers 5, 747-758.

567 Gaboury, D., 2013. Does gold in orogenic deposits come from pyrite in deeply buried carbon-rich
568 sediments?: Insight from volatiles in fluid inclusions. Geology 41, 1207-1210.

569 Goldfarb, R.J., Groves, D.I., 2015. Orogenic gold: Common or evolving fluid and metal sources through
570 time. Lithos 233, 2-26.

571 Goldfarb, R.J., Groves, D.I., Gardoll, S., 2001. Orogenic gold and geologic time: a global synthesis. Ore
572 Geology Reviews 18, 1-75.

573 Goldfarb, R.J., Santos, M., 2014. The dilemma of the Jiaodong gold deposits: Are they unique?
574 Geoscience Frontiers 5, 139-153.

575 Grosch, E.G., McLoughlin, N., 2013. Paleoarchean sulfur cycle and biogeochemical surface conditions on
576 the early Earth, Barberton, South Africa. Earth and Planetary Science Letters 377–378, 142-154.

577 Groves, D., 1993. The crustal continuum model for late-Archaean lode-gold deposits of the Yilgarn
578 Block, Western Australia. Mineralium Deposita 28, 366-374.

579 Groves, D.I., Phillips, G.N., 1987. The genesis and tectonic control on Archaean gold deposits of the
580 Western Australian Shield - A metamorphic replacement model. Ore Geology Reviews 2, 287-322.

581 Harris, P.D., Robb, L.J., Tomkinson, M.J., 1995. The nature and structural setting of rare-element
582 pegmatites along the northern flank of the Barberton greenstone belt, South Africa. South African Journal of
583 Geology 98, 82-94.

584 Hofmann, A., 2005. The geochemistry of sedimentary rocks from the Fig Tree Group, Barberton
585 greenstone belt: Implications for tectonic, hydrothermal and surface processes during mid-Archaean times.
586 Precambrian Research 143, 23-49.

587 Hofmann, A., Bekker, A., Dirks, P., Gueguen, B., Rumble, D., Rouxel, O., 2014. Comparing
588 orthomagmatic and hydrothermal mineralization models for komatiite-hosted nickel deposits in Zimbabwe
589 using multiple-sulfur, iron, and nickel isotope data. Mineralium Deposita 49, 75-100.

590 Hronsky, J., Groves, D., Loucks, R., Begg, G., 2012. A unified model for gold mineralisation in
591 accretionary orogens and implications for regional-scale exploration targeting methods. Mineralium Deposita
592 47, 339-358.

593 Hu, S., Evans, K., Craw, D., Rempel, K., Bourdet, J., Dick, J., Grice, K., 2015. Raman characterization of
594 carbonaceous material in the Macraes orogenic gold deposit and metasedimentary host rocks, New Zealand.
595 Ore Geology Reviews 70, 80-95.

596 Jamieson, J.W., Wing, B.A., Farquhar, J., Hannington, M.D., 2013. Neoarchaean seawater sulphate
597 concentrations from sulphur isotopes in massive sulphide ore. Nature Geoscience 6, 61-64.

598 Jiang, Z., Oliver, N.H.S., Barr, T.D., Power, W.L., Ord, A., 1997. Numerical modeling of fault-controlled
599 fluid flow in the genesis of tin deposits of the Malage ore field, Gejiu mining district, China. Economic Geology
600 92, 228-247.

601 Kakegawa, T., Ohmoto, H., 1999. Sulfur isotope evidence for the origin of 3.4 to 3.1 Ga pyrite at the
602 Princeton gold mine, Barberton Greenstone Belt, South Africa. Precambrian Research 96, 209-224.

603 Kamo, S.L., Davis, D.W., 1994. Reassessment of Archean crustal development in the Barberton
604 Mountain Land, South Africa, based on U-Pb dating. Tectonics 13, 167-192.

605 Kendrick, M.A., Honda, M., Walshe, J., Petersen, K., 2011. Fluid sources and the role of abiogenic-CH_4 in
606 Archean gold mineralization: Constraints from noble gases and halogens. Precambrian Research 189, 313-327.

607 Kisters, A.F.M., Belcher, R.W., Poujol, M., Dziggel, A., 2010. Continental growth and convergence-
608 related arc plutonism in the Mesoarchaean: Evidence from the Barberton granitoid-greenstone terrain, South
609 Africa. Precambrian Research 178, 15-26.

610 Kisters, A.F.M., Stevens, G., Dziggel, A., Armstrong, R.A., 2003. Extensional detachment faulting and
611 core-complex formation in the southern Barberton granite-greenstone terrain, South Africa: evidence for a 3.2
612 Ga orogenic collapse. Precambrian Research 127, 355-378.

613 Kolb, J., Dziggel, A., Bagas, L., 2015. Hypozonal lode gold deposits: A genetic concept based on a review
614 of the New Consort, Renco, Hutti, Hira Buddini, Navachab, Nevoria and The Granites deposits. Precambrian
615 Research 262, 20-44.

616 Kröner, A., Byerly, G.R., Lowe, D.R., 1991. Chronology of early Archaean granite-greenstone evolution in
617 the Barberton Mountain Land, South Africa, based on precise dating by single zircon evaporation. Earth and
618 Planetary Science Letters 103, 41-54.

619 Kröner, A., Hegner, E., Wendt, J.I., Byerly, G.R., 1996. The oldest part of the Barberton granitoid-
620 greenstone terrain, South Africa: evidence for crust formation between 3.5 and 3.7 Ga. Precambrian Research
621 78, 105-124.

622 Lowe, D.R., Byerly, G.R., 2007. An overview of the geology of the Barberton greenstone belt and
623 vicinity: Implications for early crustal development, in: Kranendonk, M.J.v., Smithies, R.H., Vickie, C.B. (Eds.),
624 Earth's Oldest Rocks, pp. 481-524.

625 Lüders, V., Klemd, R., Oberthür, T., Plessen, B., 2015. Different carbon reservoirs of auriferous fluids in
626 African Archean and Proterozoic gold deposits? Constraints from stable carbon isotopic compositions of
627 quartz-hosted CO_2-rich fluid inclusions. Mineralium Deposita 50, 449-454.

628 Marin-Carbonne, J., Chaussidon, M., Boiron, M.-C., Robert, F., 2011. A combined in situ oxygen, silicon
629 isotopic and fluid inclusion study of a chert sample from Onverwacht Group (3.35 Ga, South Africa): New
630 constraints on fluid circulation. Chemical Geology 286, 59-71.

631 Marin-Carbonne, J., Rollion-Bard, C., Bekker, A., Rouxel, O., Agangi, A., Cavalazzi, B., Wohlgemuth-
632 Ueberwasser, C.C., Hofmann, A., McKeegan, K.D., 2014. Coupled Fe and S isotope variations in pyrite nodules
633 from Archean shale. Earth and Planetary Science Letters 392, 67-79.

634 Mikucki, E.J., Ridley, J.R., 1993. The hydrothermal fluid of Archaean lode-gold deposits at different
635 metamorphic grades: compositional constraints from ore and wallrock alteration assemblages. Mineralium
636 Deposita 28, 469-481.

637 Montinaro, A., Strauss, H., Mason, P.R.D., Roerdink, D., Münker, C., Schwarz-Schampera, U., Arndt, N.T.,
638 Farquhar, J., Beukes, N.J., Gutzmer, J., Peters, M., 2015. Paleoarchean sulfur cycling: Multiple sulfur isotope
639 constraints from the Barberton Greenstone Belt, South Africa. Precambrian Research 267, 311-322.

640 Mumin, A.H., Fleet, M.E., 1995. Evolution of gold mineralization in the Ashanti Gold Belt, Ghana:
641 Evidence from carbonate compositions and parageneses. Mineralogy and Petrology 55, 265-280.

642 Munyai, M.R., Dirks, P.H.G.M., Charlesworth, E.G., 2011. Archaean gold mineralisation during post-
643 orogenic extension in the New Consort gold mine, Barberton Greenstone Belt, South Africa. South African
644 Journal of Geology 114, 121-144.

645 Ono, S., Eigenbrode, J.L., Pavlov, A.A., Kharecha, P., Rumble Iii, D., Kasting, J.F., Freeman, K.H., 2003.
646 New insights into Archean sulfur cycle from mass-independent sulfur isotope records from the Hamersley
647 Basin, Australia. Earth and Planetary Science Letters 213, 15-30.

648 Otto, A., Dziggel, A., Kisters, A., Meyer, F., 2007. The New Consort Gold Mine, Barberton greenstone
649 belt, South Africa: orogenic gold mineralization in a condensed metamorphic profile. Mineralium Deposita 42,
650 715-735.

651 Penniston-Dorland, S.C., Mathez, E.A., Wing, B.A., Farquhar, J., Kinnaird, J.A., 2012. Multiple sulfur
652 isotope evidence for surface-derived sulfur in the Bushveld Complex. Earth and Planetary Science Letters 337–
653 338, 236-242.

654 Philippot, P., Van Zuilen, M., Lepot, K., Thomazo, C., Farquhar, J., Van Kranendonk, M.J., 2007. Early
655 Archaean microorganisms preferred elemental sulfur, not sulfate. Science 317, 1534-1537.

656 Philippot, P., van Zuilen, M., Rollion-Bard, C., 2012. Variations in atmospheric sulphur chemistry on early
657 Earth linked to volcanic activity. Nature Geoscience 5, 668-674.

658 Phillips, G.N., Groves, D.I., Kerrich, R., 1996. Factors in the formation of the giant Kalgoorlie gold
659 deposit. Ore Geology Reviews 10, 295-317.

660 Phillips, G.N., Powell, R., 2009. Formation of gold deposits: Review and evaluation of the continuum
661 model. Earth-Science Reviews 94, 1-21.

662 Pitcairn, I.K., Teagle, D.A.H., Craw, D., Olivo, G.R., Kerrich, R., Brewer, T.S., 2006. Sources of metals and
663 fluids in orogenic gold deposits: insights from the Otago and Alpine Schists, New Zealand. Economic Geology
664 101, 1525-1546.

665 Pokrovski, G.S., Akinfiev, N.N., Borisova, A.Y., Zotov, A.V., Kouzmanov, K., 2014. Gold speciation and
666 transport in geological fluids: Insights from experiments and physical-chemical modelling, Geological Society
667 Special Publication, pp. 9-70.

668 Qiu, Y., McNaughton, N.J., 1999. Source of Pb in orogenic lode-gold mineralisation: Pb isotope
669 constraints from deep crustal rocks from the southwestern Archaean Yilgarn Craton, Australia. Mineralium
670 Deposita 34, 366-381.

671 Ridley, J., Mikucki, E.J., Groves, D.I., 1996. Archean lode-gold deposits: fluid flow and chemical evolution
672 in vertically extensive hydrothermal systems. Ore Geology Reviews 10, 279-293.

673 Rogers, A.J., Kolb, J., Meyer, F.M., Vennemann, T., 2013. Two stages of gold mineralization at Hutti
674 mine, India. Mineralium Deposita 48, 99-114.

675 Roerdink, D.L., Mason, P.R.D., Farquhar, J., Reimer, T., 2012. Multiple sulfur isotopes in Paleoarchean
676 barites identify an important role for microbial sulfate reduction in the early marine environment. Earth and
677 Planetary Science Letters 331-332, 177-186.

678 Roerdink, D.L., Mason, P.R.D., Whitehouse, M.J., Reimer, T., 2013. High-resolution quadruple sulfur
679 isotope analyses of 3.2 Ga pyrite from the Barberton Greenstone Belt in South Africa reveal distinct
680 environmental controls on sulfide isotopic arrays. Geochimica et Cosmochimica Acta 117, 203-215.

681 Roerdink, D.L., Mason, P.R.D., Whitehouse, M.J., Brouwer, F.M., 2016. Reworking of atmospheric sulfur
682 in a Paleoarchean hydrothermal system at Londozi, Barberton Greenstone Belt, Swaziland. Precambrian
683 Research 280, 195-204.

684 Salier, B.P., Groves, D.I., McNaughton, N.J., Fletcher, I.R., 2005. Geochronological and stable isotope
685 evidence for widespread orogenic gold mineralization from a deep-seated fluid source at ca 2.65 Ga in the
686 Laverton Gold Province, Western Australia. Economic Geology 100, 1363-1388.

687 Schoene, B., de Wit, M.J., Bowring, S.A., 2008. Mesoarchean assembly and stabilization of the eastern
688 Kaapvaal craton: A structural-thermochronological perspective. Tectonics 27, TC5010.

689 Schouwstra, R.P., 1995. Wall-rock alteration as a guide to gold-bearing fracture zones in the
690 Zwartkoppie Section, Sheba gold mine, South Africa. South African Journal of Geology 98, 399-414.

691 Seward, T.M., 1973. Thio complexes of gold and the transport of gold in hydrothermal ore solutions.
692 Geochimica et Cosmochimica Acta 37, 379-399.

693 Sibson, R.H., 2004. Controls on maximum fluid overpressure defining conditions for mesozonal
694 mineralisation. Journal of Structural Geology 26, 1127-1136.

695 Simon, G., Huang, H., Penner-Hahn, J.E., Kesler, S.E., Kao, L.-S., 1999. Oxidation state of gold and arsenic
696 in gold-bearing arsenian pyrite. American Mineralogist 84, 1071-1079.

697 Steadman, J.A., Large, R.R., Meffre, S., Olin, P.H., Danyushevsky, L.V., Gregory, D.D., Belousov, I., Lounejeva,
698 E., Ireland, T.R., Holden, P., 2015. Synsedimentary to early diagenetic gold in black shale-hosted pyrite nodules at
699 the Golden Mile deposit, Kalgoorlie, Western Australia. Economic Geology 110, 1157-1191.

700 Thomas, H.V., Large, R.R., Bull, S.W., Maslennikov, V., Berry, R.F., Fraser, R., Froud, S., Moye, R., 2011.
701 Pyrite and pyrrhotite textures and composition in sediments, laminated quartz veins, and reefs at Bendigo gold
702 mine, Australia: Insights for ore genesis. Economic Geology 106, 1-31.

703 Thomassot, E., Cartigny, P., Harris, J.W., Lorand, J.P., Rollion-Bard, C., Chaussidon, M., 2009.
704 Metasomatic diamond growth: A multi-isotope study (^{13}C, ^{15}N, ^{33}S, ^{34}S) of sulphide inclusions and their host
705 diamonds from Jwaneng (Botswana). Earth and Planetary Science Letters 282, 79-90.

706 Tomkins, A.G., 2010. Windows of metamorphic sulfur liberation in the crust: Implications for gold
707 deposit genesis. Geochimica et Cosmochimica Acta 74, 3246-3259.

708 Tomkins, A.G., 2013. A biogeochemical influence on the secular distribution of orogenic gold. Economic
709 Geology 108, 193-197.

710 Van Kranendonk, M.J., 2011. Cool greenstone drips and the role of partial convective overturn in
711 Barberton greenstone belt evolution. Journal of African Earth Sciences 60, 346-352.

712 Viljoen, M.J., Viljoen, R.P., 1969. Introduction to the geology of the Barberton granite-greenstone
713 terrain. Geological Society of South Africa Special Publication 2, 9-28.

714 Wagener, J.H.F., Wiegand, J., 1986. The Sheba Gold Mine, Barberton Greenstone Belt, in: Anhaeusser,
715 C.R., Maske, S. (Eds.), Mineral Deposits of Southern Africa Vol.I. Geol. Soc. South Africa, pp. 155-161.

716 Wang, L.G., McNaughton, N., Groves, D., 1993. An overview of the relationship between granitoid
717 intrusions and gold mineralisation in the Archaean Murchison Province, Western Australia. Mineralium
718 Deposita 28, 482-494.

719 Xue, Y., Campbell, I., Ireland, T.R., Holden, P., Armstrong, R., 2013. No mass-independent sulfur isotope
720 fractionation in auriferous fluids supports a magmatic origin for Archean gold deposits. Geology 41, 791-794.

721 Yardley, B.W.D., Cleverley, J.S., 2013. The role of metamorphic fluids in the formation of ore deposits.
722 Geological Society, London, Special Publications 393.

723 Wulff, K., Dziggel, A., Kolb, J., Vennemann, T., Böttcher, M.E., Meyer, F.M., 2010. Origin of mineralizing fluids
724 of the sediment-hosted Navachab Gold Mine, Namibia: Constraints from stable (O, H, C, S) isotopes. Economic
725 Geology 105, 285-302.

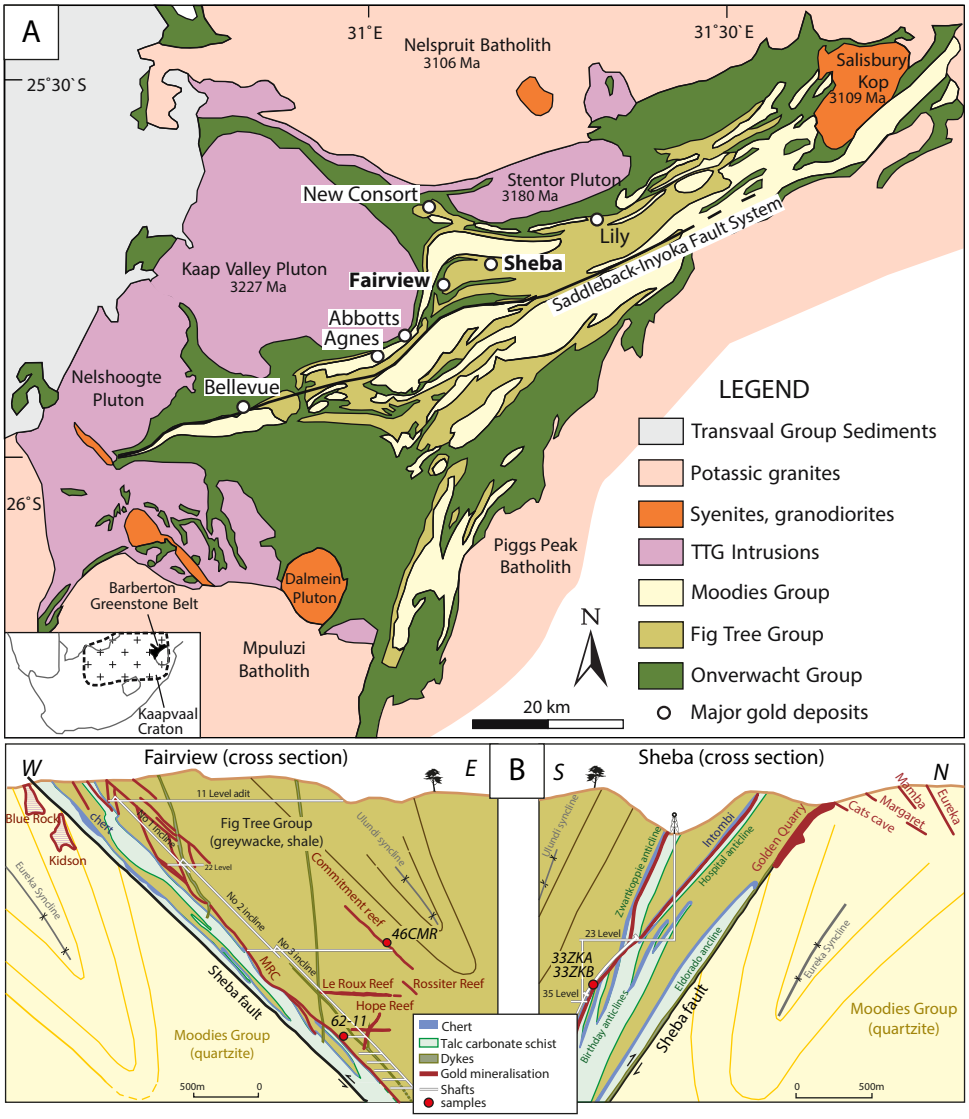

Fig.1 A Geological map of the Barberton Greenstone Belt and distribution of the main gold deposits (Modified from De Ronde et al., 1992). B and C Cross-sections of Fairview and Sheba mines (modified from Barberton mines, 2015).

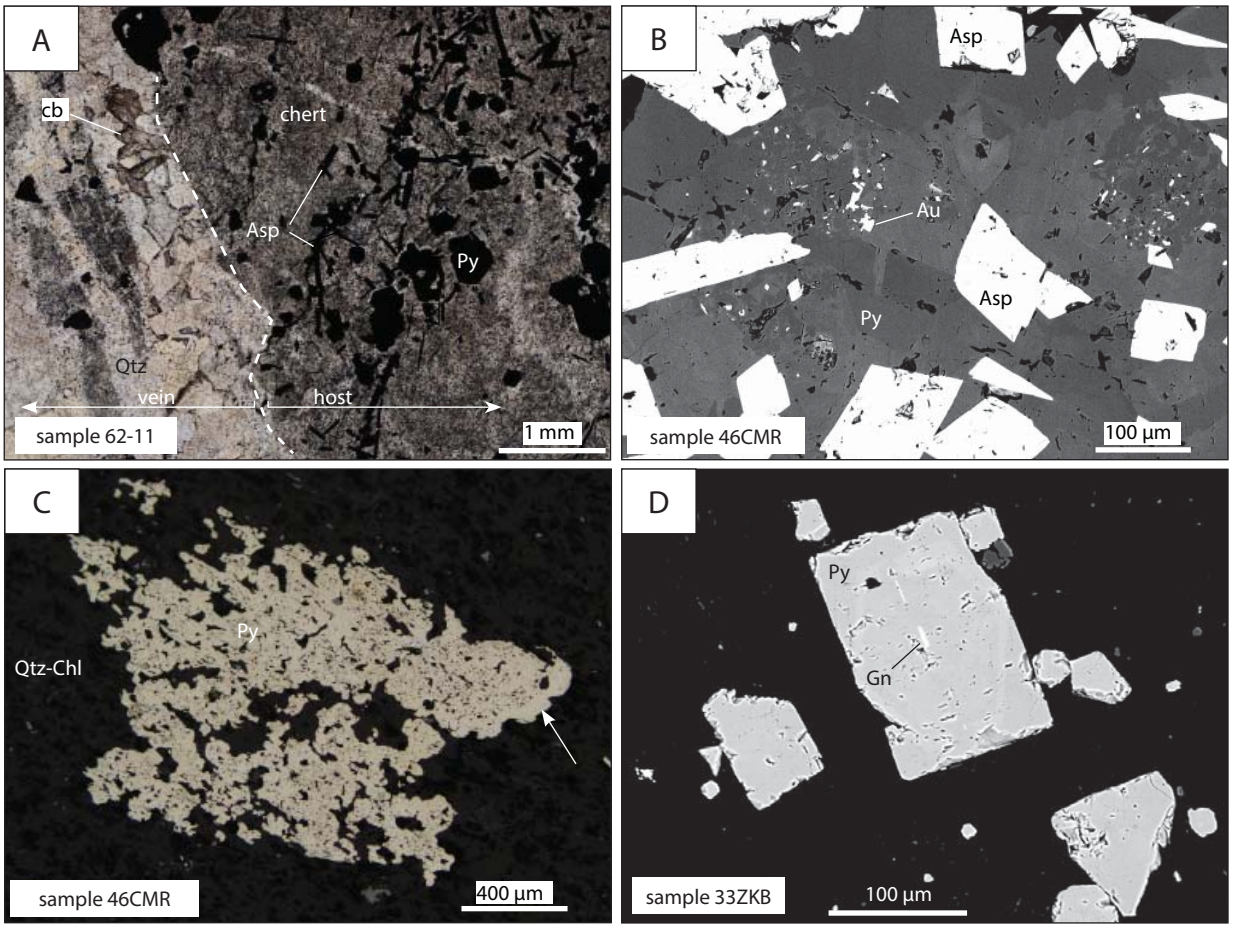
A
cb
chert
Asp
Py
Qtz
vein
host
sample 62-11
1 mm
B
Asp
Au
Py
Asp
sample 46CMR
100 µm
C
Py
Qtz-Chl
sample 46CMR
400 µm
D
Py
Gn
sample 33ZKB
100 µm

Fig 2

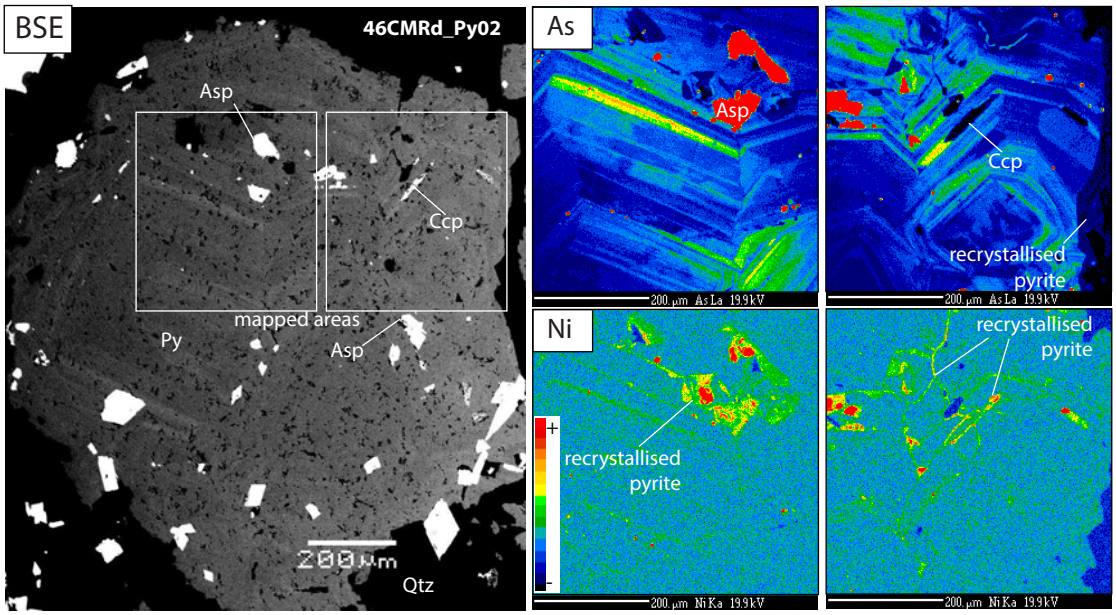
BSE
46CMRd_Py02
Asp
Ccp
mapped areas
Py
Asp
200µm
Qtz
As
Asp
Ccp
recrystallised
pyrite
Ni
recrystallised
pyrite
recrystallised
pyrite

Fig 3

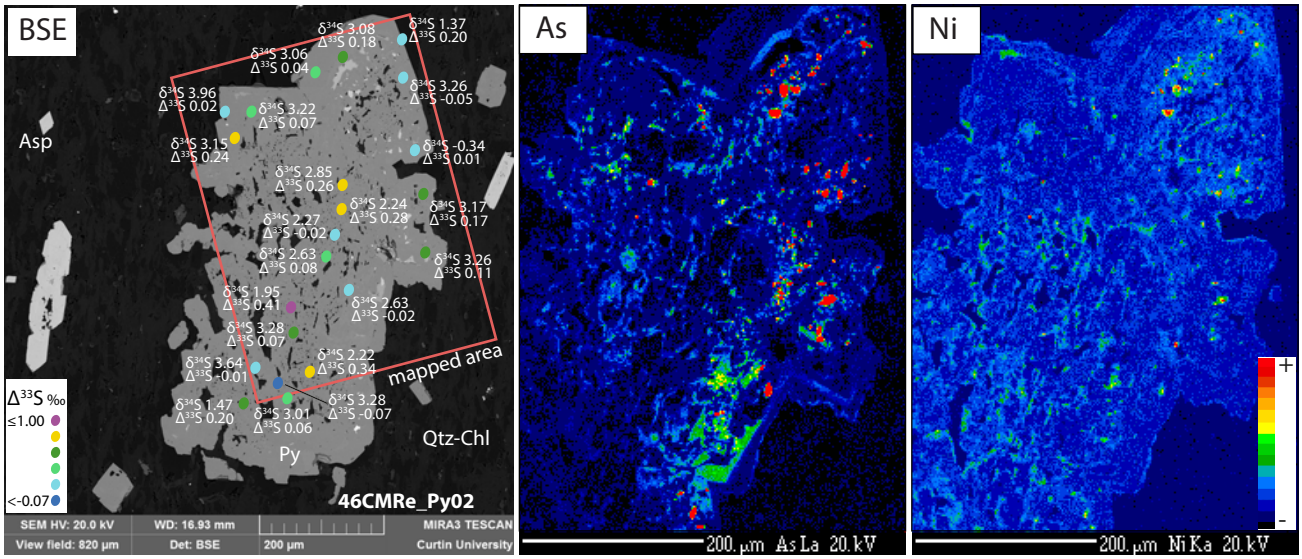
BSE
Asp
Py
Qtz-Chl
mapped area
46CMRe_Py02
Δ33S ‰
≤1.00
<-0.07
SEM HV: 20.0 kV
WD: 16.93 mm
MIRA3 TESCAN
View field: 820 μm
Det: BSE
200 μm
Curtin University
As
200 μm As La 20 kV
Ni
200 μm Ni Ka 20 kV

Fig 4

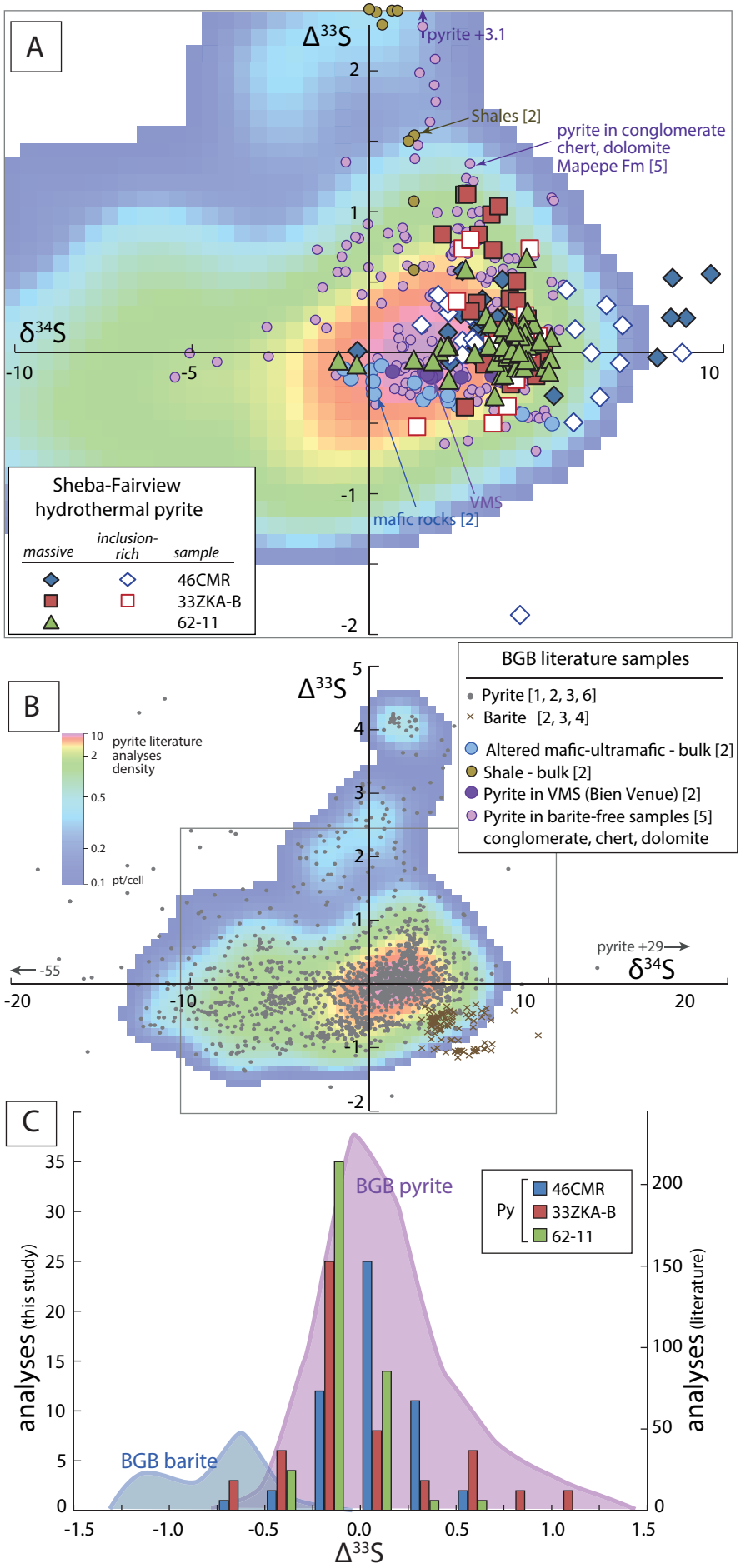

Fig 5 Multiple S isotope plots of pyrite from Sheba and Fairview mines. A and B Plot of Δ33S vs. δ34S. C Frequency histogram of Δ33S. The Ddata are compared with pyrite, and barite and bulk-rock analyses from various units of the Barberton Greenstone Belt, some groups of literature analyses are differentiated to exemplify specific distributions (data from Bao et al., 2007; Grosch and McLoughlin, 2013; Montinaro et al., 2015; Philippot et al., 2012; Roerdink et al., 2012; 2013; 2016). Density distribution of literature pyrite analyses was calculated as number of spots per ~0.5 δ34S × 0.1 Δ33S cell. Literature analyses acquired with different bulk and in situ methods, uncertainty up to ~0.5 ‰ δ34S, 0.2 ‰. References [1] Philippot et al. (2012), [2] Montinaro et al. (2015), [3] Roerdink et al. (2012), [4] Bao et al. (2007), [5] Roerdink et al. (2013), [6] Grosch and McLoughlin(2013)

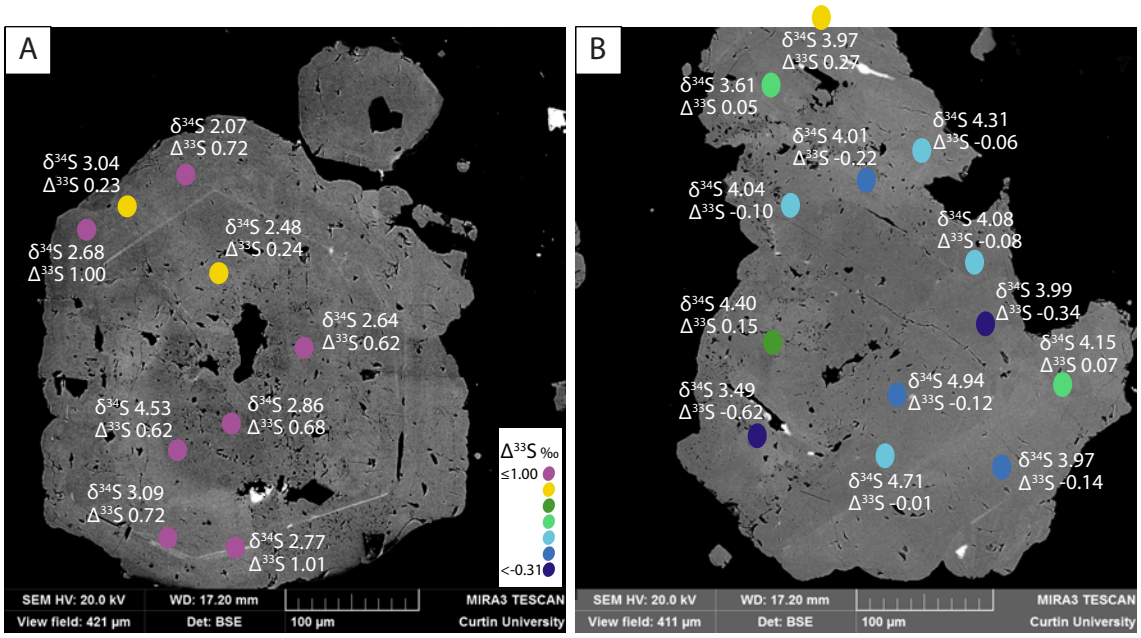
A
δ34S 2.07
Δ33S 0.72
δ34S 3.04
Δ33S 0.23
δ34S 2.68
Δ33S 1.00
δ34S 2.48
Δ33S 0.24
δ34S 2.64
Δ33S 0.62
δ34S 4.53
Δ33S 0.62
δ34S 2.86
Δ33S 0.68
δ34S 3.09
Δ33S 0.72
δ34S 2.77
Δ33S 1.01
Δ33S ‰
≤1.00
<-0.31
SEM HV: 20.0 kV
WD: 17.20 mm
MIRA3 TESCAN
View field: 421 µm
Det: BSE
100 µm
Curtin University
B
δ34S 3.97
Δ33S 0.27
δ34S 3.61
Δ33S 0.05
δ34S 4.01
Δ33S -0.22
δ34S 4.31
Δ33S -0.06
δ34S 4.04
Δ33S -0.10
δ34S 4.08
Δ33S -0.08
δ34S 3.99
Δ33S -0.34
δ34S 4.40
Δ33S 0.15
δ34S 4.15
Δ33S 0.07
δ34S 3.49
Δ33S -0.62
δ34S 4.94
Δ33S -0.12
δ34S 4.71
Δ33S -0.01
δ34S 3.97
Δ33S -0.14
SEM HV: 20.0 kV
WD: 17.20 mm
MIRA3 TESCAN
View field: 411 µm
Det: BSE
100 µm
Curtin University

Fig 6

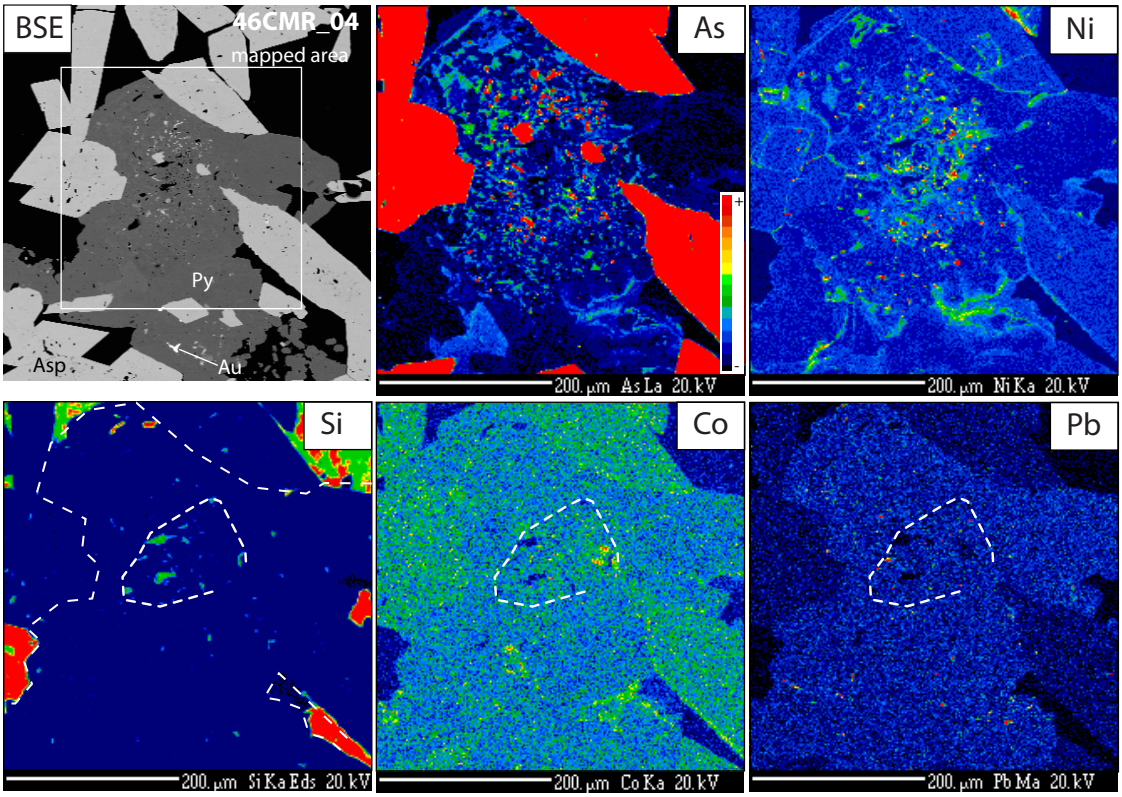
BSE
46CMR_04
- mapped area
Py
Asp
Au
As
200. µm As La 20.kV
Ni
200. µm Ni Ka 20.kV
Si
200. µm Si Ka Eds 20.kV
Co
200. µm Co Ka 20.kV
Pb
200. µm Pb Ma 20.kV

Add Fig 1

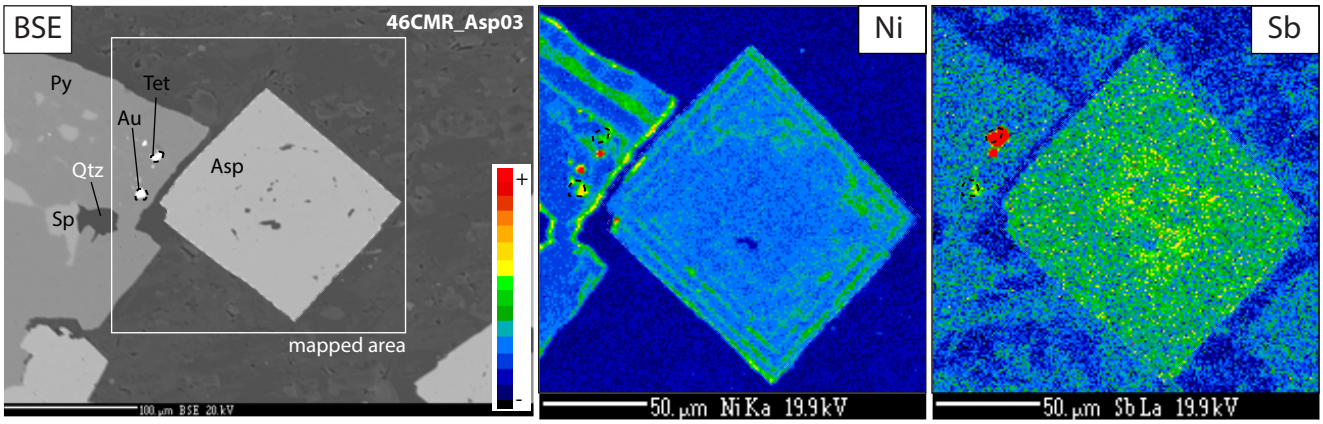
BSE
46CMR_Asp03
Py
Tet
Au
Qtz
Asp
Sp
mapped area
+
-
100 µm BSE 20 kV
Ni
50 µm Ni Ka 19.9 kV
Sb
50 µm Sb La 19.9 kV

Add Fig 2

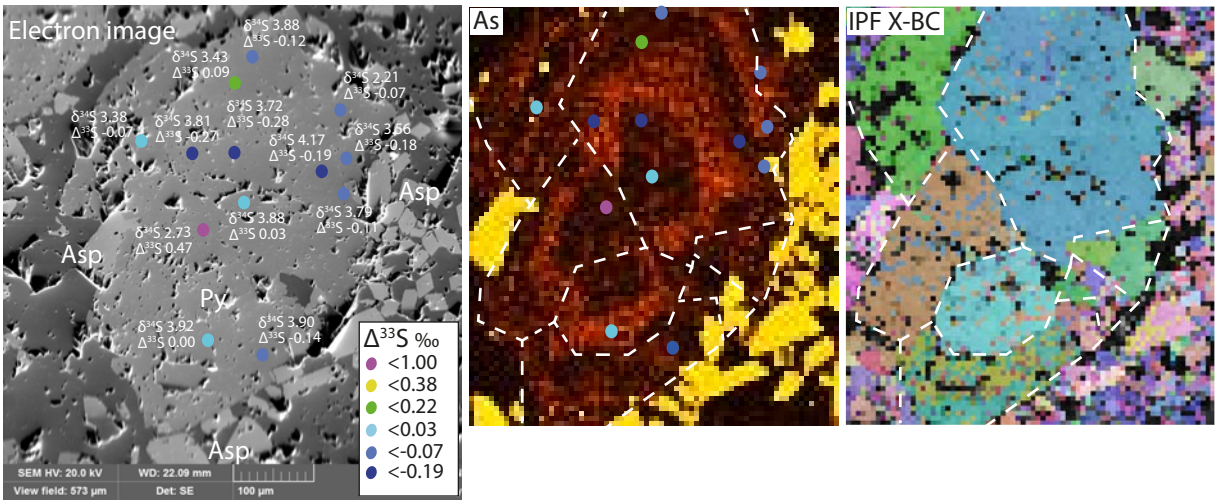
Electron image
δ34S 3.88
Δ33S -0.12
δ34S 3.43
Δ33S 0.09
δ34S 2.21
Δ33S -0.07
δ34S 3.38
Δ33S -0.07
δ34S 3.81
Δ33S -0.27
δ34S 3.72
Δ33S -0.28
δ34S 4.17
Δ33S -0.19
δ34S 3.66
Δ33S -0.18
Asp
δ34S 3.79
Δ33S -0.11
δ34S 3.88
Δ33S 0.03
δ34S 2.73
Δ33S 0.47
Asp
Py
δ34S 3.92
Δ33S 0.00
δ34S 3.90
Δ33S -0.14
Δ33S ‰
<1.00
<0.38
<0.22
<0.03
<-0.07
<-0.19
Asp
SEM HV: 20.0 kV
WD: 22.09 mm
View field: 573 µm
Det: SE
100 µm
As
IPF X-BC

Add Fig 3

Additional Table 1. Results of S isotope analyses of pyrite (SIMS)

sample	analysis ID	texture	δ33S ‰	err	δ34S ‰	err	Δ33S ‰
46CMR	46CMR-e@1	compact	1.55	0.07	3.10	0.08	-0.16
46CMR	46CMR-e@02	compact	1.60	0.07	3.13	0.08	-0.12
46CMR	46CMR-e@06	compact	1.11	0.08	2.29	0.09	-0.19
46CMR	46CMR-e@07	compact	1.29	0.07	2.22	0.09	0.02
46CMR	46CMR-e@11	compact	2.20	0.06	3.78	0.07	0.14
46CMR	46CMR-e@12	compact	1.55	0.07	2.99	0.10	-0.10
46CMR	46CMR-e@13	compact	1.82	0.06	3.44	0.08	-0.07
46CMR	46CMR-e@15	compact	1.74	0.07	3.10	0.08	0.03
46CMR	46CMR-e@16	compact	2.02	0.05	3.19	0.10	0.26
46CMR	46CMR-e@17	compact	1.93	0.08	2.63	0.07	0.46
46CMR	46CMR-e@18	compact	2.45	0.06	3.76	0.07	0.40
46CMR	46CMR-e@19	compact	1.60	0.06	2.58	0.07	0.16
46CMR	46CMR-e@21	compact	1.60	0.10	3.04	0.11	-0.08
46CMR	46CMR-e@22	compact	1.89	0.07	3.13	0.08	0.17
46CMR	46CMR-e@25	compact	2.11	0.09	3.62	0.07	0.13
46CMR	46CMR-e@26	compact	2.03	0.08	3.83	0.08	-0.05
46CMR	46CMR-e@29	compact	2.06	0.64	3.98	0.15	-0.11
46CMR	46CMR-e@30	compact	1.63	0.08	3.26	0.06	-0.17
46CMR	46CMR-e@31	compact	1.77	0.08	3.08	0.07	0.07
46CMR	46CMR-e@32	compact	1.61	0.08	3.06	0.07	-0.08
46CMR	46CMR-e@33	compact	-0.16	0.06	-0.34	0.10	-0.11
46CMR	46CMR-e@35	compact	1.81	0.06	3.17	0.08	0.06
46CMR	46CMR-e@36	compact	1.79	0.07	3.26	0.09	0.00
46CMR	46CMR-e@37	compact	1.73	0.08	3.22	0.09	-0.04
46CMR	46CMR-e@38	compact	2.06	0.09	3.96	0.09	-0.09
46CMR	46CMR-e@39	compact	1.86	0.07	3.15	0.08	0.12
46CMR	46CMR-e@42	porous	1.73	0.06	2.85	0.07	0.14
46CMR	46CMR-e@43	porous	1.44	0.10	2.24	0.08	0.16
46CMR	46CMR-e@44	porous	1.15	0.07	2.27	0.09	-0.14
46CMR	46CMR-e@45	porous	1.44	0.05	2.63	0.08	-0.03
46CMR	46CMR-e@46	porous	1.34	0.05	2.63	0.07	-0.13
46CMR	46CMR-e@47	porous	1.41	0.07	1.95	0.09	0.29
46CMR	46CMR-e@48	porous	1.60	0.06	2.92	0.08	-0.02
46CMR	46CMR-e@50	porous	1.49	0.08	2.22	0.06	0.23
46CMR	46CMR-e@51	porous	1.61	0.06	3.28	0.07	-0.19
46CMR	46CMR-e@52	porous	1.87	0.07	3.64	0.05	-0.12
46CMR	46CMR-e@53	porous	0.96	0.09	1.48	0.10	0.08
46CMR	46CMR-e@54	porous	1.61	0.08	3.01	0.09	-0.05
46CMR	46CMR-e@55	porous	3.78	0.08	6.70	0.05	0.22
46CMR	46CMR-e@56	porous	3.87	0.13	7.15	0.06	0.08
46CMR	46CMR-e@57	porous	3.16	0.11	5.82	0.05	0.05
46CMR	46CMR-e@58	porous	4.54	0.10	8.83	0.05	-0.11
46CMR	46CMR-e@59	compact	4.14	0.13	8.14	0.06	-0.15
46CMR	46CMR-e@60	compact	4.84	0.11	8.94	0.07	0.14
46CMR	46CMR-e@61	compact	4.93	0.15	8.56	0.09	0.42
46CMR	46CMR-e@62	compact	4.63	0.16	8.52	0.09	0.14
46CMR	46CMR-e@63	compact	5.51	0.20	9.64	0.07	0.45
46CMR	46CMR-e@64	porous	3.22	0.17	6.27	0.11	-0.11
46CMR	46CMR-e@65	compact	2.37	0.21	5.21	0.10	-0.42
46CMR	46CMR-e@66	porous	3.03	0.24	6.52	0.05	-0.43
46CMR	46CMR-e@67	porous	3.56	0.30	7.08	0.08	-0.19
46CMR	46CMR-e@68	porous	3.31	0.24	5.57	0.08	0.33
46CMR	46CMR-e@69	porous	2.47	0.27	5.77	0.07	-0.61
46CMR	46CMR-e@70	porous	0.33	0.36	4.26	0.11	-1.98
33ZKA	33ZKA-c@1	compact	2.02	0.10	3.97	0.06	-0.14

Additional Table 1 (continued). Results of S isotope analyses of pyrite (SIMS)

33ZKA	33ZKA-c@02	compact	2.32	0.07	4.15	0.05	0.07
33ZKA	33ZKA-c@03	compact	1.83	0.10	3.99	0.08	-0.34
33ZKA	33ZKA-c@04	compact	2.13	0.08	4.08	0.04	-0.08
33ZKA	33ZKA-c@05	porous	2.27	0.07	4.31	0.05	-0.06
33ZKA	33ZKA-c@06	compact	2.42	0.12	3.97	0.05	0.27
33ZKA	33ZKA-c@07	compact	2.02	0.10	3.61	0.05	0.05
33ZKA	33ZKA-c@08	porous	1.96	0.10	4.01	0.04	-0.22
33ZKA	33ZKA-c@09	porous	2.09	0.08	4.04	0.03	-0.10
33ZKA	33ZKA-c@10	porous	2.53	0.08	4.40	0.05	0.15
33ZKA	33ZKA-c@11	porous	1.30	0.11	3.50	0.06	-0.62
33ZKA	33ZKA-c@12	compact	2.54	0.08	4.94	0.05	-0.12
33ZKA	33ZKA-c@13	compact	2.53	0.08	4.71	0.05	-0.01
33ZKA	33ZKA-c@14	compact	2.20	0.09	4.22	0.05	-0.09
33ZKA	33ZKA-c@15	compact	2.51	0.09	4.17	0.05	0.25
33ZKA	33ZKA-c@16	compact	1.96	0.11	4.13	0.05	-0.28
33ZKA	33ZKA-c@17	compact	2.17	0.09	4.13	0.06	-0.07
33ZKA	33ZKA-c@18	compact	1.98	0.06	4.15	0.05	-0.27
33ZKA	33ZKA-c@19	compact	2.30	0.08	4.60	0.04	-0.18
33ZKA	33ZKA-c@20	compact	2.25	0.09	4.20	0.05	-0.03
33ZKA	33ZKA-c@21	compact	2.17	0.10	4.20	0.05	-0.10
33ZKA	33ZKA-c@22	porous	0.17	0.08	1.35	0.09	-0.65
33ZKA	33ZKA-c@23	compact	1.00	0.09	2.70	0.11	-0.51
33ZKA	33ZKA-c@24	compact	1.59	0.08	3.25	0.10	-0.20
33ZKA	33ZKA-c@25	compact	2.13	0.08	4.22	0.06	-0.15
33ZKA	33ZKA-c@26	compact	2.26	0.08	4.71	0.06	-0.28
33ZKA	33ZKA-c@27	porous	2.58	0.06	4.78	0.07	0.00
33ZKA	33ZKA-c@28	compact	2.54	0.06	4.47	0.04	0.13
33ZKA	33ZKA-c@29	compact	2.12	0.09	4.24	0.06	-0.18
33ZKA	33ZKA-c@30	porous	1.94	0.06	4.15	0.07	-0.31
33ZKA	33ZKA-c@31	porous	1.84	0.06	3.47	0.08	-0.06
33ZKA	33ZKA-c@32	porous	2.13	0.07	4.31	0.07	-0.20
33ZKA	33ZKA-c@33	porous	1.63	0.06	3.90	0.06	-0.50
33ZKA	33ZKA-c@34	porous	2.16	0.07	4.08	0.06	-0.06
33ZKA	33ZKA-c@35	porous	2.11	0.06	4.01	0.05	-0.07
33ZKA	33ZKA-c@36	porous	2.35	0.07	4.42	0.06	-0.04
33ZKA	33ZKA-c@37	porous	2.12	0.08	3.95	0.06	-0.03
33ZKA	33ZKA-c@38	porous	1.97	0.07	3.90	0.07	-0.15
33ZKA	33ZKA-c@39	porous	2.32	0.07	4.47	0.06	-0.09
33ZKA	33ZKA-c@40	compact	1.92	0.14	3.04	0.06	0.23
33ZKA	33ZKA-c@41	compact	2.50	0.14	2.68	0.06	1.00
33ZKA	33ZKA-c@42	compact	1.90	0.17	2.07	0.05	0.72
33ZKA	33ZKA-c@43	porous	1.64	0.16	2.48	0.04	0.24
33ZKA	33ZKA-c@44	porous	2.09	0.16	2.64	0.07	0.62
33ZKA	33ZKA-c@45	porous	2.27	0.15	2.86	0.05	0.68
33ZKA	33ZKA-c@46	porous	3.07	0.19	4.53	0.05	0.62
33ZKA	33ZKA-c@47	compact	2.42	0.18	3.09	0.09	0.72
33ZKA	33ZKA-c@48	compact	2.55	0.21	2.77	0.08	1.01
33KZB	33KZB@1	compact	1.94	0.09	3.90	0.06	-0.18
33KZB	33KZB@2	compact	1.93	0.05	3.65	0.05	-0.07
33KZB	33KZB@3	compact	1.77	0.10	2.86	0.06	0.17
33KZB	33KZB@4	compact	2.75	0.08	3.45	0.06	0.86
33KZB	33KZB@5	compact	2.92	0.09	3.65	0.07	0.92
33KZB	33KZB@6	compact	2.53	0.06	3.50	0.07	0.61
33KZB	33KZB@7	compact	2.65	0.09	4.17	0.06	0.39
62-11	62-11@04	compact	1.03	0.09	1.98	0.07	-0.11
62-11	62-11@05	compact	1.96	0.05	3.29	0.07	0.14

Additional Table 1 (continued). Results of S isotope analyses of pyrite (SIMS)

62-11	62-11@06	compact	1.51	0.05	3.54	0.06	-0.43
62-11	62-11@07	compact	0.97	0.12	2.25	0.10	-0.31
62-11	62-11@08	compact	1.08	0.10	2.03	0.04	-0.08
62-11	62-11@09	compact	1.52	0.07	2.98	0.05	-0.12
62-11	62-11@10	compact	1.21	0.09	2.25	0.05	-0.07
62-11	62-11@11	compact	1.93	0.07	3.92	0.06	-0.20
62-11	62-11@12	compact	0.60	0.10	1.26	0.15	-0.17
62-11	62-11@13	compact	-0.51	0.08	-0.87	0.11	-0.18
62-11	62-11@14	compact	-0.26	0.10	-0.35	0.08	-0.21
62-11	62-11@15	compact	0.86	0.11	1.80	0.11	-0.18
62-11	62-11@16	compact	1.99	0.11	3.88	0.06	-0.12
62-11	62-11@17	compact	1.97	0.06	3.43	0.07	0.09
62-11	62-11@18	compact	1.75	0.09	3.72	0.06	-0.28
62-11	62-11@19	compact	1.80	0.11	3.81	0.06	-0.27
62-11	62-11@20	compact	1.79	0.10	3.38	0.06	-0.07
62-11	62-11@21	compact	1.18	0.09	2.21	0.06	-0.07
62-11	62-11@22	compact	1.77	0.09	3.56	0.06	-0.18
62-11	62-11@23	compact	2.07	0.09	4.17	0.06	-0.19
62-11	62-11@24	compact	1.96	0.07	3.79	0.08	-0.11
62-11	62-11@25	compact	2.15	0.07	3.88	0.05	0.03
62-11	62-11@26	compact	1.99	0.07	2.73	0.06	0.47
62-11	62-11@27	compact	2.13	0.09	3.92	0.06	0.00
62-11	62-11@28	compact	1.98	0.09	3.90	0.06	-0.14
62-11	62-11@32	compact	2.02	0.07	3.90	0.07	-0.10
62-11	62-11@33	compact	2.13	0.09	4.20	0.09	-0.14
62-11	62-11@34	compact	2.75	0.09	5.14	0.05	0.00
62-11	62-11@35	compact	2.45	0.04	4.96	0.06	-0.22
62-11	62-11@36	compact	2.51	0.06	4.76	0.06	-0.05
62-11	62-11@37	compact	2.59	0.09	5.12	0.06	-0.16
62-11	62-11@38	compact	2.47	0.09	5.07	0.06	-0.25
62-11	62-11@39	compact	2.59	0.09	4.65	0.06	0.08
62-11	62-11@40	compact	2.23	0.08	3.90	0.07	0.11
62-11	62-11@41	compact	2.59	0.09	4.47	0.06	0.18
62-11	62-11@42	compact	2.22	0.06	3.95	0.07	0.08
62-11	62-11@43	compact	2.08	0.05	3.79	0.06	0.02
62-11	62-11@44	compact	2.20	0.05	3.92	0.07	0.06
62-11	62-11@45	compact	2.96	0.08	4.44	0.06	0.56
62-11	62-11@46	compact	2.44	0.06	4.35	0.05	0.08
62-11	62-11@47	compact	2.40	0.08	4.40	0.05	0.02
62-11	62-11@48	compact	2.35	0.04	4.47	0.06	-0.06
62-11	62-11@49	compact	2.03	0.08	4.15	0.06	-0.22
62-11	62-11@53	compact	1.99	0.07	3.79	0.05	-0.07
62-11	62-11@54	compact	2.04	0.04	3.99	0.06	-0.12
62-11	62-11@55	compact	2.26	0.09	4.51	0.06	-0.18
62-11	62-11@59	compact	2.09	0.09	4.29	0.07	-0.22
62-11	62-11@60	compact	2.15	0.06	4.38	0.06	-0.22
62-11	62-11@61	compact	2.09	0.05	4.04	0.05	-0.10
62-11	62-11@62	compact	2.13	0.07	3.79	0.05	0.07
62-11	62-11@63	compact	2.31	0.06	4.26	0.06	0.00
62-11	62-11@64	compact	2.22	0.12	4.42	0.06	-0.17
62-11	62-11@65	compact	2.56	0.08	4.83	0.05	-0.03
62-11	62-11@66	compact	2.18	0.05	4.24	0.06	-0.11
62-11	62-11@67	compact	2.26	0.07	4.10	0.05	0.03